広島大学学位請求論文

Interaction mechanisms of small unilamellar vesicle and monoclonal antibody targeting to oxidized LDL receptor protein LOX-1

（酸化 LDL 受容体タンパク質 LOX-1 を標的にする小型単層ベシクルおよびモノクローナル抗体の相互作用メカニズム）

２０１９年

広島大学大学院理学研究科

数理分子生命理学専攻

大田　哲也

目　次

主論文

Interaction mechanisms of small unilamellar vesicle and monoclonal antibody targeting to oxidized LDL receptor protein LOX-1

Tetsuya Ohta

Department of Mathematical and Life sciences

Graduate School of Science

Hiroshima University

2019

Contents

Chapter I　General Introduction

I-1. Onset mechanism of atherosclerosis by oxidized LDL hypothesis

Myocardial and cerebral infarction are currently the main causes of deaths in the world's demographics [1], and they are mainly caused by atherosclerosis. Historically, "response-to-injury hypothesis" [2] or “response-to-retention hypothesis” [3] were proposed to explain a mechanism of atherogenesis, however, "oxidized LDL hypothesis” [4] described below is being supported as the most potent atherogenic mechanism in recent years [5].

Oxidized low density lipoprotein (OxLDL) is taken up into vascular endothelial cell by the specific receptors expressing on the cell surface, and activates multiple inflammatory signal pathways causing endothelial cell dysfunction. It promotes LDL and monocyte in the blood to adhere to vascular endothelial cells, and to infiltrate into intima. LDL changes to OxLDL, and monocytes differentiate into macrophages in intima. Macrophages uptake large amounts of OxLDL through phagocytosis then change to foam cells. As this accumulates in intima, fatty streaks are formed and become atheroma plaques. Dysfunctional endothelial cells and foam cells due to OxLDL produce and secrete various inflammatory cytokines, growth factors, and adhesion factors. They promote smooth muscle cells migration into the intima. Along with these cascade, intimal thickness and lipid deposition in artery occur, and plaque growth progresses. Plaque ruptures eventually, and a thrombus is formed. Finally, blood flow decreases due to stenosis or occlusion in blood vessels, causing a cardiovascular accident [6,7].

I-2. Oxidized LDL receptor protein; LOX-1

Lectin-like OxLDL receptor-1 (LOX-1) (gene name; *OLR1*) was found as a major OxLDL receptor expressing on vascular endothelial cells [8]. It is a membrane glycoprotein of about 50 kDa consisting of 273 amino acids. The C-terminal extracellular domain is named C-type lectin-like domain (CTLD) [9], forms a homodimer and functions as an OxLDL binding site [10,11]. LOX-1 is highly expressed in atherosclerotic plaque lesions in the early stages of atherogenesis [12], and internalizes OxLDL into cells by clathrin-independent endocytic pathway [13–15]. Previous studies on X-ray crystal structure of LOX-1 CTLD homodimer have proposed the interaction mechanism for OxLDL binding [16–20]. OxLDL binding interface on CTLD exposes some positively charged arginine residues which have a characteristic arrangement named "basic spine" [16]. LOX-1 CTLD recognizes not only OxLDL and modified LDLs [5] but also various substances including advanced glycation end products (AGEs) [21], and C-reactive protein (CRP) [22] etc. Thus,

LOX-1 plays a major role in the progression of the early stages of atherosclerosis.

I-3. Relationship between LOX-1 and cancer, autoimmune disorder, and other diseases

In recent years, previous studies reporting that LOX-1 is associated with not only atherosclerosis [5] but also tumorigenesis [23–25] are increasing [26]. LOX-1 is up-regulated in several different types of malignant tumor. For example, in colorectal cancer cells, LOX-1 level increases significantly, which correlates with cancer cell growth rate and invasiveness [23]. Furthermore, large Japanese epidemiological cohort studies have also demonstrated that serum OxLDL levels correlate with the risk of developing colorectal cancer [27]. These evidences link colorectal cancer with LOX-1. Similarly, serum OxLDL levels are positively correlated with breast and ovarian cancer risk [27]. LOX-1 seems to be involved in tumorigenesis by stimulating angiogenesis [28–30]. LOX-1 acted as an enhancer of tumor angiogenesis in prostate cancer [24,31]. Liang *et al.* have reported that LOX-1 mediates the adhesion and trans-endothelial migration of breast cancer cells, and promotes the breast cancer metastasis [32]. Importantly, It has been demonstrated in the article that the adhesion of breast cancer cells to endothelial cells and the trans-endothelial migration could be blocked by both the anti-LOX-1 antibody and the recombinant LOX-1 protein [32]. LOX-1 also promotes the development and progression of gastric cancer [33], and pancreatic cancer through epithelial- mesenchymal transition [34]. Previous epidemiological research has shown that a combination of LOX-1 expression levels and degrees of obesity for individual patients is a prognostic prediction factor for squamous non-small cell lung cancer [35] . Thus, it is clear that LOX-1 is becoming an important part of oncology research.

Also, there seems to be a link between LOX-1 and autoimmune disorder. Akagi *et al.* have reported that LOX-1 is also associated with osteoarthritis and cartilage degeneration [36]. OxLDL binding to LOX-1 enhances monocyte chemoattractant protein 1 (MCP-1) expression in cultured human articular chondrocytes, however, it was suppressed markedly by anti-human LOX-1 monoclonal antibody (mAb) [36]. LOX-1 seems to be a potent biomarker and therapeutic target for rheumatoid arthritis [37] .

As for hypercholesterolemia, there are reports that the expression levels of proprotein convertase subtilisin/kexin type 9 (PCSK9) and LOX-1 positively correlate [38]. PSCK9 promotes lysosomal degradation of LDL receptor, and increases serum LDL level. Selective PCSK9 inhibition by anti-PCSK9 mAb; evolocumab and alirocumab, which have been approved to be launched as biopharmaceutical by FDA and EMA in 2015, has emerged as a novel lipid-lowering therapy to treat hypercholesterolemia and associated diseases [39]. The combination of LOX-1 inhibition may further enhance its PCSK9 targeting therapeutic effect. Thus, the importance of drug discovery research targeting LOX-1 is increasing more and more.

I-4. Prior drug discovery research targeting LOX-1

The accumulation of many previous studies [7] convinces us that LOX-1 is a promising drug target for the treatment and prevention of the above diseases, however, there are no LOX-1 selective inhibitors or drug delivery system (DDS) carriers that can be used clinically. Various artificial substances targeting LOX-1 have developed to date. They include synthetic small molecule compounds [40,41], monoclonal antibodies (mAbs) [8,42], single chain variable fragment (ScFv) [43], radioisotope (^{99m}Tc) labeled mAb [44], mAb conjugated immunoliposome [45,46], antisense oligonucleotide [47], DNA nanocage [48], and so on. Vigorous research activities aimed at clinical application are being continued [7,49,50]. The development of better LOX-1 selective inhibitors or DDS carriers will present new treatments for the above mentioned diseases.

I-5. Purpose and structure of this doctoral dissertation

In this doctoral dissertation, two different types of artificial ligands specifically bind to LOX-1 were focused on, and their interaction mechanisms with LOX-1 were studied. One is anionic liposome (small unilamellar vesicle), and the other is monoclonal antibody (mAb). This is because these are promising agents for LOX-1 targeting therapy.

In chapter II, the feasibility of nano-liposomes as LOX-1 selective DDS carrier was investigated and discussed based on a pharmaceutical science approach. Small unilamellar vesicles (SUVs) composed of negatively charged phospholipid DOPG or neutrally charged phospholipid DOPC were prepared in different sizes, and their affinities toward LOX-1 on SPR sensor chip or living cell surface were evaluated.

In chapter III, I focused on a chicken-derived anti-LOX-1 mAb, named as HUC52. It binds to human LOX-1 CTLD and inhibits uptake of OxLDL. It has two cysteine residues capable of forming disulfide bond in the third complementarity-determining region of heavy chain (CDR-H3). Since this is a rare sequence in human or mouse-derived mAbs, HUC52 may form a special CDR-H3 conformation. Three-dimensional structure models of the Fab domain, and its interaction mechanism with CTLD homodimer were estimated by using computer simulation techniques.

Chapter IV summarizes finally the findings obtained in this research.

Chapter II DOPG small unilamellar vesicles function as nano-carriers targeting the clustered lectin-like oxidized LDL receptor (LOX-1) on the cell surface

II-1. Introduction

LOX-1 localizes to caveolae/lipid rafts of the cell membrane by subjecting its cytoplasmic domain to palmitoyl modification [15,51], and internalizes OxLDL ligands into cells by caveolae/raft-dependent [15], or clathrin-independent endocytosis pathway [13,14]. The basal LOX-1 expression level is low in cells under physiological conditions, whereas it is upregulated in dysfunctional cells under pathological conditions, and increases the uptake of OxLDLs [52–54]. That is, LOX-1 expression is an obvious biomarker for cell dysfunction in the progression of atherosclerosis [5,55].

Several previous studies have revealed the structure and the ligand binding mechanism of LOX-1 CTLD homodimer [16,20,56]. The CTLD has the 'basic spine structure' comprising an array of arginine residues on the dimer surface (Fig. II-1), and it explains the preferential binding of LOX-1 to negatively charged ligands such as OxLDL [16,17,56,57]. LOX-1 homodimer units on the cell membrane can self-associate, and exist as higher order irregular oligomers (it is described as a "cluster" in this chapter), consisting of tetramer (two homodimer units), hexamer (three homodimer units), or possibly more [52,58]. Surface plasmon resonance (SPR) experiments in the previous study by Ohki *et al*. have demonstrated that biotinylated LOX-1 CTLD clusters reconstituted on streptavidin coated sensor bound to OxLDL in a multivalent manner, and exerted 10^4 to 10^5 times stronger affinity toward OxLDL when compared with the homodimer alone [19]. Cao *et al*. have also reported that LOX-1 oligomerization of tetramer or higher with an orientation of the interfaces of all the CTLDs in the same direction is essential for high-affinity binding to OxLDL by using a LOX-1 CTLD-IgG Fc fusion proteins cross-linked with anti-Fc antibody to form CTLD octamers at maximum [59]. These evidences suggest that the clustering state of LOX-1 on the cell membrane and orientation control of CTLD strongly influence the ligand uptake activity.

Despite the importance, the detailed structure and functions of the clustering LOX-1 are still almost unknown. There are various questions to be elucidated, for example, how LOX-1 clusters interacts with OxLDL multivalently, and what is the correlation between the number of associated LOX-1 molecules and the OxLDL affinity. Although the exact clustering state and numbers of LOX-1 expressing on atherosclerotic plaque or cancer cells are still elusive, understanding them in detail would lead to the creation of inhibitors or drug delivery

system (DDS) carriers that selectively target to LOX-1 cluster with a stronger affinity than OxLDL.

Native LDL comprises ApoB-100 as the only protein constituent [17]. Oxidation of LDL modifies lysine and arginine residues in ApoB-100 by removing their positive side chain charges to form OxLDL, which has an overall negative charge [60]. The zeta-potential of LDL changes from -8 to -21 mV following oxidation, which happens during storage of LDL over four weeks [61]. The more oxidized LDL would increase affinity toward LOX-1 on cells because of an increase in the number of electrostatic interactions between the OxLDL and the basic spine structure on the CTLD of LOX-1.

Nanoparticles (NPs) represented by liposome are expected to be suitable template of DDS carrier targeting LOX-1 cluster because of their similar shape and size to OxLDL. Then, it was envisaged that NPs with negative charge greater than OxLDL would function as a selective ligand to LOX-1 clusters on cells. Several liposome DDS therapeutic agents such as Doxil® are already in clinical use as commercial products [62,63]. The development of nanoparticle DDS carriers is at the forefront of DDS research and is a rapidly progressing area [64]. Despite the growing importance of LOX-1 as a therapeutic target, there are only a few reports describing NPs that target LOX-1 [45,46,48].

In this chapter, the feasibility of nano-liposomes as LOX-1 selective DDS carrier was investigated and discussed. Specifically, anionic small unilamellar vesicles (SUVs) composed of negatively charged phospholipid DOPG (1,2-dioleoyl-*sn*-glycero-3-[phospho-*rac*-(1-glycerol)]) or neutrally charged phospholipid DOPC (1,2-dioleoyl-*sn*-glycero-3-phosphocholine) were prepared in various sizes. Their affinities toward LOX-1 clusters were compared by SPR experiments. The SPR sensor chips were designed to immobilize LOX-1 extracellular domain (ECD) on a self-assembled monolayer (SAM) so as to mimic the clustering state of LOX-1s on the cell membrane (Fig. II-2). In addition, competitive cellular uptake assays for fluorescently labeled DOPG-SUV and acetylated LDL (AcLDL, a chemically stable surrogate reference substance equivalent to OxLDL) into LOX-1 expressing CHO cells were conducted to evaluate which is preferentially internalized into the cells.

II-2. Materials and methods

II-2-1. Materials

Lipids used for making small unilamellar vesicles (SUV); DOPG (1,2-dioleoyl-*sn*-glycero-3-[phospho-rac-(3-lysl(1-glycerol))]) (Fig. II-3 A) and DOPC (1,2-dioleoyl-*sn*-glycero-3-phosphocholine) (Fig. II-3 B), and 30, 100 nm sizing filters were purchased from Avanti Polar Lipids, Inc. (Alabaster, AL, USA). The fluorescent probe DiI (1,1'-dioctadecyl-1 to 3,3,3',3'-tetramethylindocarbocyanine per-chlorate) and DiD (1,1′-dioctadecyl-3,3,3′,3′-tetramethylindocarbocyanine per-chlorate) were purchased from Invitrogen (Carlsbad,

CA, USA). AcLDL was purchased from Biomedical Technologies (Stoughton, MA, USA). The self-assembled monolayer (SAM) used in the SPR experiments was prepared with OEG-OH (Hydroxy-EG3-undecanethiol) (Dojindo Laboratories, Kumamoto, Japan) and OEG-NTA (HS-$(CH_2)_{11}$-EG3-NTA) (ProChimia Surfaces, Gyand, Poland). The CHO cell line was obtained from RIKEN Cell Bank (Tsukuba, Japan).

II-2-2. Preparation of LOX-1 extracellular domain fragment

Recombinant LOX-1 extracellular domain (ECD; residues 61–273) fused His_6-tag at its N-terminus was expressed in *Escherichia coli* (*E.coli*) cells, prepared by refolding from the inclusion bodies, and purified according to the procedure described before [16,19]. The LOX-1 ECD protein used for SPR experiments was retained His_6-tag for anchoring it to the sensor chip. The prepared LOX-1 ECD was confirmed to be in a disulfide linked homodimer by SDS-PAGE.

II-2-3. Preparation of small unilamellar vesicles (SUVs)

A 100 μL chloroform solution containing 5 mg of DOPG (Fig. II-3 A) or DOPC (Fig. II-3 B) in glass tube was subjected to N_2 gas flow to evaporate the solvent. The solvent-purged lipid was further dried in a desiccator connected to a vacuum pump for ~12 hours. The extensively dried lipid sample in a glass tube was dispersed in 1 mL solution to be used in the intended experiments by vigorous mixing and kept at room temperature for 30 min. For fluorescence labeling to SUV, 32 μL of DiI DMSO solution (50 mg/ml) was added at this step. The solution was vigorously mixed by vortexing. The glass tube was immersed in liquid nitrogen to make the lipid film inside the glass tube, and then the frozen lipid film was thawed in a warm bath at 42°C. This freeze-thaw cycle was repeated for five times.

The prepared liposome solution was then subjected to sizing to make unilamellar vesicles with the extruding device (Avanti Polar Lipids, Inc.). Two types of sizing polycarbonate membrane filter, 30 nm or 100 nm in pore diameter were used to give the unilamellar vesicles in different sizes. Extruding the liposome solution between two connected syringes was repeated at least 90 times through the membrane to make SUVs in a narrow size distribution with polydispersity index (PDI) less than 0.2. Hereafter, DOPG-SUV prepared with 30 nm filter is abbreviated as “DOPG-SUV30”. Similarly, DOPG-SUV prepared with 100 nm filter is abbreviated as “DOPG-SUV100”, and DOPC-SUV prepared with 30 nm filter is abbreviated as “DOPC-SUV30”, respectively.

The hydrodynamic diameters, surface potentials (zeta potentials), and PDI of the SUVs dispersed in ultra-pure water (Merck-Millipore KGaA, Darmstadt, Germany) were measured with dynamic light scattering (DLS) using Zetasizer Nano (Malvern Instruments Ltd.).

The prepared SUVs were stored in water at 25 °C. The physicochemical stability of DOPG-SUV30 was monitored at the time points of 1, 47, 71, 93 and 109 days after preparation.

The statistical errors for each particle size and surface potential were estimated as the standard deviations

through the serially repeated triplicate experiments.

II-2-4. SPR measurement

II-2-4-1. Preparation of the SPR sensor chip coating NTA self-assembled monolayer (SAM)

In this experiments, the self-assembled monolayer (SAM) on SPR sensor chip was made of 10% OEG-NTA and 90% OEG-OH. The NTA moiety in OEG-NTA is used to anchor LOX-1 ECD fusing HIS_6-tag at its N-terminus (Fig. II-2). The SAM coated SPR sensor chip was prepared in the following procedure.

The gold thin plate, SIA-Kit Au (GE Healthcare) was sank into the Piranha solution comprising of 30 mL H_2O_2 and 70 mL conc. H_2SO_4. The gold plate was kept in the solution for 30 min to generate clean gold surface. The gold plate was extensively rinsed by ultra-pure water and then dried up by blowing dried N_2 gas on its surface. The cleaned gold plate was immediately put in the 2 mL solution containing 0.1 mM OEG-NTA and 0.9 mM OEG-OH in dark at room temperature for 24 hours. The SAM coated gold plate was carefully washed with ethanol four times then dried by blowing the air onto the surface. The SAM coated gold plate was mounted onto the Biacore sensor frame and kept in dark at 4°C until it is used. The SAM sensor was prepared just prior to every experiment.

II-2-4-2. SPR experiments of SUVs with LOX-1 ECD clusters anchored to the SAM sensor

SPR experiments were performed by using Biacore X system (GE Healthcare, Buckingham, UK) and SPR02 system (Optoquest Co.Ltd., Tokyo, Japan). LOX-1 EDC was dissolved in the buffer A (10 mM HEPES, pH 7.4, 150 mM NaCl) to give 100 μg/mL concentration. The NTA group on the SAM sensor was activated by loading Ni^{2+} ions with 20 μL flow of 0.5 M $NiCl_2$ in buffer A. LOX-1 ECD was immobilized by flowing 40 μL LOX-1 ECD solution onto the Ni-loaded SAM at the flow rate of 10 μL /min. LOX-1 ECD was immobilized up to in the range from 4000 to 4500 resonance unit (RU). After washing the sensor surface with 80 μL buffer B (10 mM HEPES, pH 7.4, 150 mM NaCl, 50 μM EDTA), the analytes dissolved in the buffer B were flowed to the sensor chip. For the binding of AcLDL to LOX-1 ECD, 250 μL of AcLDL solution was flowed at 5 μL /min. In using SUVs, 100 μL analyte solution was flowed at 20 μL /min. All the experiments were carried out at 25°C.

Equilibrium dissociation constants (K_D) values were estimated from the equilibrium data at the ends of the adsorbing phase sensorgrams without using kinetic analysis [19]. Accurate kinetic analysis was not possible because the classical one-to-one binding model is inappropriate due to the multivalent interaction between the ligands and the clustered LOX-1 ECD on the sensor surface.

The statistical errors for each K_D value were estimated by co-variances in fitting calculations with the program Scrubber-2 (BioLogic Software, Campbell, Australia).

II-2-5. Competitive cellular uptake assay of DOPG-SUV30 and AcLDL using LOX-1 expressing

cells

DiI-labeled DOPG-SUV was prepared as described above. The used DOPG-SUV was sized with the 30 nm pore diameter membrane filter (DiI-DOPG-SUV30). DiD-AcLDL was prepared as described before [52]. In this uptake experiments, CHO cell line expressing stably cyan fluorescent protein (CFP) tagged LOX-1 at the level to elicit AcLDL uptake (T-CHO cells) [52] was used. Cells grown on cover slides were incubated with DiD-AcLDL and DiI-DOPG-SUV30 in defined amounts for 10 min on ice. The final concentration of DiD-AcLDL in the cell medium ranged from 0.4 μg/mL to 8.0 μg/mL, while the concentration of DiI-DOPG-SUV30 was changed from 0.25 μM to 5.0 μM. The excessed DiD-AcLDL and DiI-DOPG-SUV30 were gently washed out with fresh cold medium without fetal calf serum (FCS). The cells were then chemically fixed with a 2% formaldehyde/PBS (-) solution. Each cover slip was mounted onto a glass slide.

The treated cells were measured with a Leica DM IRE2 microscope (Leica Microsystems, Wetzler, Germany) equipped with a ×100, NA 1.4 objective and a Cool SNAP HQ digitized cooled CCD camera (Roper Scientific, Trenton, NJ) controlled by MetaMorph software (Universal Imaging, Downingtown, PA). The fluorescence derived from CFP was measured using an E4 filter with excitation at 436 nm (7-nm bandpass) and a 470-nm long-pass emission filter. The DiD-AcLDL derived fluorescence was measured using an Y5 filter with excitation at 620 nm (50 nm bandpass) and a 700 nm (75 nm bandpass) emission filter. For detecting DiI-DOPG-SUV30, the fluorescence was measured using an Y3 filter, with excitation at 535 nm (50-nm bandpass) and a 610 nm (75 nm bandpass) emission filter. All images were acquired at 0.1 sec exposures. The input amounts of AcLDL and DOPG-SUV30 were compared in molar units using the molecular weights estimated for each of them, as described below.

The molecular weight of AcLDL was assumed to be the same as for LDL reported in the literature, 2.5×10^6 Da [65], because the particle size of AcLDL is very close to those of LDL and OxLDL [66]. The number of DOPG molecules per single DOPG-SUV30 particle was estimated as 2.3×10^4 on the basis of the geometric requirements in a lipid vesicle bilayer [67]. In the calculation, we assumed the average volume per lipid molecule (the specific volume) of DOPG to be the same as that for phosphatidylcholine [67], which is acceptable because they share similar alkyl chain chemical structures. The thicknesses of the outer and inner monolayers in the DOPG-SUV30 were also assumed to be the same as those for a phosphatidylcholine SUV, i.e., 2.1 nm (outer) and 1.6 nm (inner) [67]. The molecular weight of DOPG-SUV30 was estimated to be 1.8×10^7 Da.

II-2-6. VCAM-1 induction assay

Human aortic endothelial cells (HAEC) were cultured in medium containing 10% FCS for 5 h before adding DiI-OxLDL (1.6 nM) or DiI-DOPG-SUV30 (25 pM). After the addition of DiI-OxLDL or DiI-DOPG-SUV30 into the HAEC culture in 0.2% FCS, the cells were cultured for 16 h before chemical fixation of the cells using

2% formaldehyde in PBS (-), i.e., phosphate buffer saline without calcium and magnesium. The chemically fixed cells were incubated with anti-vascular cell adhesion molecule-1 (VCAM-1) antibody at 5 μg/mL (Rabbit polyclonal; Abcam, Cambridge, UK) for 2 h at room temperature. The cells were then incubated for another 1 h at room temperature in PBS(-) containing 10% FCS and anti-rabbit IgG labeled with Alexa Fluor 633 at 5 μg/ml (Molecular Probes, Eugene, OR, USA). The fluorescence derived from Alexa Fluor 633 was observed with the fluorescence microscope above. In the experiments, HAEC were not permeabilized, and the antibodies stained VCAM-1 expressed on the cell surface.

II-3. Results

II-3-1. Optimization of LOX-1 immobilized SAM-SPR sensor chip

In this study, to analyze quantitatively the affinities between SUVs and LOX-1 cluster, SPR sensor chip was designed to make LOX-1s on the sensor closer to the state on the cell membrane by introducing NTA self-assembled monolayer (SAM) composed of OEG-NTA and OEG-OH. N-terminal His_6-tagged LOX-1 ECD containing CTLD and NECK domain was immobilized on the sensor chip by anchoring to OEG-NTA. On this sensor surface, LOX-1 ECDs were aligned unidirectionally as envisaged for LOX-1 receptors on the cell surface (Fig. II-2).

The OEG-NTA content was optimized through SPR sensorgram responses upon binding of LOX-1 ECD to the SAM surface preliminarily. Data were collected with SPR02 system (Optoquest Co.Ltd.) at 25 °C (Fig. II-4). In a series of experiments using 0.3 to 50% OEG-NTA content in the SAM, the results for the 10% content of OEG-NTA indicated complete coverage by LOX-1 ECDs without cryptic attenuation of SPR responses. Increasing the OEG-NTA content above 10% (25 and 50%) did not lead to a uniform increase in sensor response. These observations suggest that there should be steric clashes among the LOX-1 ECDs on the SAM surface because of receptor overcrowding when OEG-NTA contents above 25% are used. LOX-1 receptors on the cell surface may also need space to neighboring receptors to allow for rearrangement of the CTLDs to tightly capture vesicles with various sizes. Overcrowding of LOX-1 ECDs on the sensor surface will not properly mimic the state of LOX-1 clusters on cells. Therefore, the 10% OEG-NTA content was chosen in the present work.

A specific SPR response arisen from AcLDL (a chemically stable surrogate reference substance equivalent to OxLDL) binding was observed only in the SAM sensor with LOX-1 ECD. On the other hand, The SAM-sensor without LOX-1 ECD showed negligible response to AcLDL, indicating that the SAM surface does not display non-specific binding toward AcLDL (Fig. II-5).

II-3-2. The size and surface charge of SUV determine the binding affinity to LOX-1 cluster

Negatively charged liposome; DOPG-SUV was prepared with 30 or 100 nm pore sizing filters (DOPG-SUV30, DOPG-SUV100) respectively, and neutrally charged liposome; DOPC-SUV was also prepared with a 30 nm pore filter (DOPC-SUV30). The size distributions and surface charges (zeta-potentials) of these SUVs and AcLDL were measured by dynamic light scattering (Fig. II-6). The binding affinities of these to LOX-1 ECD clusters on SAM sensor were measured by using Biacore X system (GE Healthcare) (Fig. II-7). The resulting sizes (hydrodynamic diameters), zeta-potentials, and dissociation constants (K_D) with LOX-1 ECD clusters of these ligands are listed in Table II-1.

AcLDL was used as a surrogate reference substance more chemically stable than OxLDL in order to avoid the influence on the reproducibility of the measurement result arising from the oxidation level heterogeneity found in OxLDL. AcLDL and OxLDL are known to have comparable binding affinity to LOX-1 [57]. The hydrodynamic diameter of AcLDL was 38.2 nm, and the zeta potential was -41.0 mV. The affinity for LOX-1 was K_D of 95×10^{-12} M (Fig. II-7 A).

The zeta potential of the DOPG-SUV30 (-42.2 mV) was close to that of AcLDL. Its size was 70.6 nm in hydrodynamic diameter, which was twice size relative to AcLDL. DOPG-SUV30 showed $K_D = 5.0 \times 10^{-12}$ M (Fig. II-7 B), it was almost 20 times stronger affinity toward LOX-1 ECD clusters when compared with that of AcLDL. Therefore, the observed difference in their affinities toward LOX-1 ECD clusters was defined by their particle sizes. DOPG-SUV30 had a larger diameter, and should interact with more LOX-1 ECDs on the sensor surface when compared with that of AcLDL, which enhances the apparent affinity of DOPG-SUV30 over AcLDL according to the number of engaged LOX-1 receptors.

DOPG-SUV100 had an average diameter of 124 nm, which was 1.8 times larger than that of DOPG-SUV30. It showed -41.6 mV zeta potential as well as DOPG-SUV30 and AcLDL. Irrespective of the larger size, DOPG-SUV100 showed only a marginal increase in affinity toward LOX-1 ECD clusters; $K_D = 3.9\times10^{12}$ M (Fig. II-7 C), when compared with that of DOPG-SUV30.

In contrast, the LOX-1 affinity loss due to the reduction of the negative charge on DOPC-SUV surface was remarkable. DOPC-SUV30 showed a diameter of 68.2 nm and -8.4 mV zeta potential. Its K_D with LOX-1 ECD clusters was 1300×10^{-12} M, and resulted in about 260 times weaker affinity to LOX-1 than DOPG-SUV30 (Fig. II-7 D). The low affinity of DOPC-SUV30 to LOX-1 ECD clusters was not unexpected because its neutral surface charge was similar to that of native LDL (-8.3 mV) that does not bind to LOX-1 [8,61].

These SPR sensorgrams obtained in this experiments were not fit to one-to-one binding model functions. This suggests that multiple LOX-1 ECDs on the sensor interact with the ligand in a multivalent manner.

II-3-3. Competitive uptake of DOPG-SUV against AcLDL via LOX-1 on cell surface

Native CHO cells expressed LOX-1 at a very low level, and uptake of DiD-labeled AcLDL or DiI-labeled

DOPG-SUV30 was not observed (Fig. II-8 A). In contrast, substantial uptakes of DiI-labeled DOPG-SUV30 and DiD-labeled AcLDL into the CHO cells stably expressing CFP-tagged LOX-1 (T-CHO cells) was observed (Fig. II-8 B) as demonstrated in previous study [52]. Therefore, uptakes of AcLDL and DOPG-SUV30 into T-CHO cells were mediated by LOX-1-dependent endocytosis.

In the presence of 1.5 times amount of DiD-labeled AcLDL, uptake of DiI-labeled DOPG-SUV30 into T-CHO cells was almost exclusive (Fig. II-9 A). In contrast, at 1.4 times amounts of DOPG-SUV30 relative to AcLDL, AcLDL uptake was almost completely abolished (Fig. II-9 B). Even in the presence of about 150-times excess AcLDL, DiI-labeled DOPG-SUV30 uptake was still observed (Fig. II-9 C). Approximately 300-times the amount of DiD-labeled AcLDL was required to completely inhibit the uptake of DOPG-SUV30 into the cells (Fig. II-9 D).

These results demonstrated that DOPG-SUV30 had a strong antagonist activity against AcLDL binding to LOX-1 clusters on cell surface and therefore prevented AcLDL uptake through LOX-1-mediated endocytosis. DOPG-SUV30 would work as a nano-DDS carrier to deliver payloads through LOX-1-dependent endocytosis pathway.

II-3-4. DOPG-SUV does not induce VCAM-1 expression

The cytotoxicity derived from DOPG-SUV30 in human aortic endothelial cell (HAEC) was assessed based on the induction level of VCAM-1 as a molecular marker for dysfunctional cells (Fig. II-10). OxLDL binding to LOX-1 induces the production of cell adhesion molecules including VCAM-1 to recruit monocytes to the endothelium to initiate atherosclerosis [49,54]. Also in this study, OxLDL induced VCAM-1 expression. In contrast, DOPG-SUV30 did not induce VCAM-1 expression. No cell deformity due to DOPG-SUV30 addition was also observed.

II-3-5. Physicochemical stability of DOPG-SUV

Changes in the physicochemical properties of DOPG-SUV30 during storage in water at 25 ℃ were monitored (Fig. II-11). The particle size became slightly larger over the first 70 days of storage, while the polydispersity index (PDI), which provides information about the particle size distribution, and surface charge changed slightly. At the time of storage at 70 days, the DOPG-SUV30 remains less than 90 nm in diameter with an improved particle size distribution (smaller PDI) and a slightly enhanced negative surface charge. On the other hand, at 93 days after preparation, the diameter of DOPG-SUV 30 increased to 120 nm. The PDI rose to 0.35 and the surface charge reached to -80 mV. These observations indicated that DOPG-SUV30 is stable for 70 days after preparation.

II-4. Discussion

II-4-1. Structure of LOX-1 ECD clusters formed on a SAM-SPR sensor

In this study, SPR sensor chips harboring LOX-1 ECD clusters on the self-assembled monolayer (SAM) surface was designed to mimics the clustering state of LOX-1s expressing on plasma membrane surface. On the sensor surface, LOX-1 ECDs are aligned unidirectionally (Fig. II-2). This LOX-1 ECD-SAM sensor showed the affinity to AcLDL with $K_D = 95\times10^{-12}$ M (Table. II-1). This value was about 40 times stronger than the previous SPR study result using biotinylated CTLD homodimer-immobilized on streptavidin-coated sensor with AcLDL ($K_D = 3.9\times10^{-9}$ M) reported by Ohki *et al.* in 2011 [19]. In addition, this is nearly 180 times stronger than OxLDL affinity ($K_D = 1.7\times10^{-8}$ M) reported for human coronary artery endothelial cells (HCAECs) expressing LOX-1 [68].

These differences in the affinities are considered due to the fact that the SAM sensor surface prepared in this study formed LOX-1 clusters plane with a higher density and a larger area than the previous SPR study or LOX-1 expressing cell surface. LOX-1 ECD was immobilized on the 10% NTA-SAM sensor chip to show a response of 4000 to 4500 resonance unit (RU). In Biacore system, the change of 1000 RU corresponds to the binding of about 1 ng/mm^2 of substance onto the sensor chip. That is, about 4 ng/mm^2 of LOX-1 ECD was immobilized on the NTA-SAM sensor chip to get a response of 4000 RU. Since an area of one measurement flow cell is 1.25 mm^2, it is calculated that about 5 ng (approximately 6×10^{10} molecules) of LOX-1 ECD covered completely the flow cell surface of the SAM-SPR sensor chip.

Native LOX-1 is localized in caveolae/lipid rafts on the plasma membrane of endothelial cells [15,51]. The diameter of lipid raft is known to be about 50 to 100 nm [69], and native LOX-1 is considered to exist mainly as tetramer or hexamer as one cluster unit [52]. Although the exact number of LOX-1 molecules expressing per one lipid raft on the cells is unknown, about several tens to at most 100 LOX-1 molecules could express there and form the clusters when calculated roughly from their sizes. The density of LOX-1 on the SAM sensor chip must be much denser than that on the native lipid raft. However the planarly clustered structure could have been reproduced faithfully. This LOX-1 ECD clusters -SAM sensor chip prepared in this study worked well as an analysis tool to detect the LOX-1 binding affinity of various SUV ligands with enhanced sensitivity.

II-4-2. Interaction between DOPG-SUVs and LOX-1 clusters on SAM-SPR sensor

Anionic liposomes with a uniform negative charge on the surface (-42 mV) equivalent to AcLDL were prepared from phospholipid DOPG in this study. DOPG-SUV30 sized to an average diameter of 70 nm showed 20 times stronger affinity to LOX-1 ECD clusters than AcLDL (Table. II-1). This is because DOPG-SUV30 had an about twice larger particle size than AcLDL, and thus more LOX-1s on the sensor bound to one DOPG-SUV30 particle multivalently than binding to AcLDL (Fig. II-12). LOX-1 CTLD is connected to a flexible NECK domain (Fig. II-1) [18], and the flexibility of the NECK domain may be able to rearrange the

CTLDs to capture ligands with various sizes synergistically.

On the other hand, the affinity of DOPG-SUV100 with a diameter of 124 nm to LOX-1 clusters was not significantly different from that of DOPG-SUV30 (Table. II-1). An enhancement of ligand binding affinity to LOX-1 clusters showed a size limit. About twice change in the diameter from 70.6 nm (DOPG-SUV30) to 124.4 nm (DOPG-SUV100) did not increase the LOX-1 affinity, as observed between AcLDL (38.2 nm) and DOPG-SUV30 (Fig. II-13). The result that both K_Ds of DOPG-SUV30 and DOPG-SUV100 were nearly equal would imply that the number of LOX-1 ECDs on SAM sensor which interacted with one DOPG-SUV100 particle was the same as in the case of DOPG-SUV30. As shown in the schematic diagram of spheres of DOPG-SUV100 and SUV30 (Fig. II-14), the larger diameter of particle, the more surface area should contact with the plane of LOX-1 clusters on sensor surface. One hypothesis to explain this is that DOPG-SUV30 and SUV100 may have different rigidities and elasticities respectively [70]. In fact, DOPG-SUV100 filtered with a 100 nm filter showed a diameter of 124 nm, while the SUV30 showed a hydrodynamic diameter of 70 nm despite being filtered with a 30 nm pore filter. This result implies that DOPG-SUV30 may be a softer and more deformable liposome than DOPG-SUV100 by being exposed to physical stress passing through a narrow membrane pore of 30 nm. DOPG-SUV30 may form a flatter spherical shape flexibly, and adhere to the sensor surface. As a result, it is inferred that the contact areas of DOPG-SUV30 and the SUV100 particles to the LOX-1 clusters plane on sensor were almost the same substantially. To clarify this, structural characterization of DOPG-SUVs using atomic force microscopy (AFM) etc. will be required [66,71]. This is an issue to be clarified in the future.

Looking at the SPR sensorgrams of DOPG-SUV30 and SUV100, their association and dissociation profiles with LOX-1 clusters plane appear to be different for both (Fig. II-7 B and C). DOPG-SUV30 saturated rapidly LOX-1 clusters plane and hardly dissociated thereafter (Fig. II-7 B). On the other hand, DOPG-SUV100 particles at the same molar concentration as DOPG-SUV30s took more times to saturate LOX-1 clusters plane than DOPG-SUV30. In addition, obvious dissociations were observed after the saturation only in the SUV100 injections (Fig. II-7 C). Focusing on the Resonance Unit (RU; Y-axis) of their SPR sensorgrams, when 35 pM DOPG-SUV30 was injected into the sensor, it reached a response of 6000 RU at saturation state (Fig. II-7 B). On the other hand, when 35 pM DOPG-SUV100 was injected into the sensor in the same way, it was limited to 5000 RU at saturation (Fig. II-7 C). In the Biacore system, a change of 1000 RU corresponds to approximately 1 ng/mm^2 of material bound onto the sensor. That is, it is calculated that DOPG-SUV100 reached the saturation with LOX-1 clusters plane in an amount of about 1 ng/mm^2 less than DOPG-SUV30.

This limited enhancement in the affinity and binding amount of DOPG-SUV100 can be ascribed to steric exclusion effect of unbound SUVs by vesicles bound to LOX-1 clusters on the sensor surface (Fig. II-15), which results in a reduced number of bound SUV100 particles to the sensor. More frequent steric clashes among DOPG-SUV100 particles might be caused on the SAM sensor than in case of DOPG-SUV30. The small

difference in the affinities between DOPG-SUV30 and SUV100 is reminiscent of the size-dependent change in the binding abilities of LDLs to the LDL receptor (LDLR) clustered on the cell surface, in which fewer larger than small LDLs were bound to the LDLRs [65]. The size-dependent change in LDL binding to LDLR clusters on the cell surface was explained by steric hindrance among the LDL particles on the receptor lattice in LDLR cluster expressed on cells (the lattice model) [65]. LOX-1 ECD clusters-SAM SPR sensor reproduced the size-exclusion effect that should occur in ligand binding to LOX-1 receptor-lattice on the cell surface.

Mukhamadiyarov *et al.* have reported that they prepared multilamellar vesicles composed of egg lecithin and cholesterol (molar ratio; 7: 5) by sizing them with using polycarbonate filters with pore sizes of 30 or 100 nm in almost the same way as in this study, and obtained two groups of the liposomes with an average diameter of 70 nm or 110 nm [72]. Although the surface charges have not been analyzed in their studies, Nguyen *et al.* have reported that liposomes composed of soy lecithin and cholesterol indicated -41.7 mV zeta potential values [73]. From this, it can be inferred that the liposomes composed of egg lecithin and cholesterol also had a negative surface charge close to the latter soy lecithin liposomes. The negative charge value was equivalent to that of DOPG-SUVs obtained in this study. The key point in the study of Mukhamadiyarov *et al.* is that they have demonstrated that 70 nm liposomes were taken up into ischemic rat cardiomyocytes about six times more efficiently than the 110 nm liposomes [72]. The authors did not discuss the involvement of LOX-1 in their experimental results, but it is already well known that LOX-1 expression is up-regulated in the myocardial ischemia lesion area [49], therefore I consider that LOX-1 was involved in the phenomena. The experimental results presented in this study that smaller (70 nm) negatively charged liposomes (DOPG-SUVs) bound more to the LOX-1 clusters plane than the larger liposomes with 124 nm, and the hypothesis above that the reason was due to the flexibility and size exclusion effect of the liposomes would support logically the previous research by Mukhamadiyarov *et al.*

From these SPR experiments, it was demonstrated that DOPG-SUV30 with an average diameter of 70 nm had a sufficient size and surface charge for strong interaction with LOX-1 clusters.

II-4-3. Mechanisms of LOX-1-mediated endocytosis of DOPG-SUV30 and OxLDL uptake inhibition

LOX-1 mediated endocytosis relies on clathrin-independent endocytosis (CIE) [13–15], which limits the vesicle size to a diameter of ~90 nm [74]. The average diameter size of DOPG-SUV30 was 70.6 nm, which was below the CIE size limit, whereas the average diameter of DOPG-SUV100 (i.e., 124.4 nm) was above the limit. Therefore, DOPG-SUV30 was evaluated the competitive cellular up-taken activity against AcLDL through LOX-1-mediated endocytosis.

Competitive cellular uptake assay using fluorescently labeled DOPG-SUV30 and AcLDL on LOX-1 expressing CHO cells revealed that DOPG-SUV30 was preferentially taken up into the cells rather than AcLDL.

Even in the presence of a 150 fold excess amount of AcLDL, DOPG-SUV30 was internalized efficiently (Fig. II-9). This suggests that DOPG-SUV30 should also have a stronger affinity with LOX-1 clusters expressing on the living cell membrane than AcLDL.

Each CIE cavity on the plasma membrane could accept only one DOPG-SUV30 particle and sterically exclude AcLDL/OxLDL binding to LOX-1 cluster on the cavity (Fig. II-16). As schematically drawn in Fig. II-16, the number of LOX-1 receptors engaged in binding to DOPG-SUV30 in the cavity for CIE would be much greater when compared with that of AcLDL/OxLDL to give DOPG-SUV30 higher affinity toward LOX-1 clusters than AcLDL/OxLDL. DOPG-SUV30 would kinetically exclude OxLDL binding to LOX-1 clusters, thereby blocking uptake of the pathogenic OxLDL into cells. Besides the antagonistic effect against OxLDL, DOPG-SUV30 can deliver therapeutic reagents through LOX-1 mediated CIE pathway to dysfunctional cells.

II-4-4. Feasibility of clinical use of DOPG-SUV as LOX-1 selective DDS carrier

The physicochemical properties of nanoparticles (NPs) such as their sizes, surface charges, shapes, and rigidities determine the cellular pathways utilized to internalize NPs [74–77]. Positively charged NPs no larger than 100 nm are internalized through clathrin-mediated endocytosis via a non-targeting process, in which the positively charged NPs interact with the negatively charged matrix formed by glycosaminoglycans on the cell surface [78]. Negatively charged particles such as OxLDL, AcLDL and DOPG-SUV30 do not interact with the negatively charged cell surface and are not internalized into cells in a non-targeting manner. Instead, these particles are up-taken exclusively through LOX-1-mediated CIE in a receptor-targeting manner. This characteristic of DOPG-SUV30 is therapeutically advantageous in delivering a payload to cells in pathological conditions, where LOX-1 expression is highly upregulated [79,80].

Safety of the internalized vesicle is an issue to consider when applying DOPG-SUV for therapeutic purposes. DOPG-SUV30 did not induce VCAM-1 expression, a biomarker of cell dysfunction. No cell deformity due to DOPG-SUV addition was also observed. Several liposome DDS therapeutics such as Doxil® are already in clinical use as commercial products [62,63]. Kapoor *et al.* have developed SUV liposome consisting of 40% DOPG and 60% DOPE (zwitterion lipid) as DDS nano-carrier of siRNA to breast cancer cells, and reported that it has no cytotoxicity, and that it was stable at least for 4 hours in serum [81]. DOPG-SUV30 used in this study would also be expected to show no cytotoxicity *in vivo* similar to these previous findings.

The physical stability of DOPG-SUV30 is another concern in the practical use. This study showed that DOPG-SUV30 was stable in water at room temperature for 70 days after preparation. While the diameter of DOPG-SUV30 increased to 120 nm at 93 days after preparation (Fig. II-11). This would be because SUVs have merged and become larger. The merged SUVs would not function as DDS nano-carriers, since ligands larger than 90 nm are not internalized by CIE due to their size limitations [74].

In considering therapeutic applications, further characterization for the safety and stability of DOPG-SUV30 under physiologically relevant conditions by animal studies etc. will be required, and this represents a future study. Taken together, it was confirmed that DOPG-SUV30 is a suitable DDS nano-carrier targeting LOX-1 at least for *in vitro* use.

II-5. Conclusions

In this chapter, small unilamellar vesicles (SUVs) composed of negatively charged phospholipid DOPG or neutrally charged phospholipid DOPC were prepared in different sizes (70 nm or 124 nm in a diameter), and their affinities toward LOX-1 ECD clusters immobilized on the self-assembled monolayer (SAM)-SPR sensor chips were compared to AcLDL (a chemically stable surrogate reference substance equivalent to OxLDL). Anionic DOPG-SUV sized with 30 nm pore diameter filter (DOPG-SUV30) (70 nm, -42 mV), which was about twice the diameter and an equivalent surface charge to AcLDL, showed about 20 times stronger affinity to LOX-1 ECD clusters than AcLDL. This explains that the enhancement of LOX-1 affinity correlated positively with the size of negatively charged ligands, and it was due to the multivalent interaction of more LOX-1s with one DOPG-SUV30 particle than with AcLDL. DOPG-SUV30 were internalized more preferentially into living cells expressing LOX-1 than AcLDL, even in the presence of a 150 fold excess amount of AcLDL.

On the other hand, DOPG-SUV100 (-42 mV, 124 nm), having the same surface charge and about twice the diameter compared to DOPG-SUV30, demonstrated almost the same LOX-1 affinity as that of DOPG-SUV30. These results indicated that the affinity with LOX-1 clusters was not further enhanced even if the particle size exceeds 70 nm. This was probably due to the difference in elasticity between DOPG-SUV30 and SUV100, which can make DOPG-SUV30 more flexible and flatter, and the fact that the more bulky DOPG-SUV100 had a larger size exclusion effect to unbound particles on LOX-1 clusters plane. This means that there is an optimum particle size (70 nm) in ligand binding onto LOX-1 clusters surface. In case of DOPC-SUV30 (-8.4 mV, 68 nm), the LOX-1 affinity was lost due to the reduction of the negative charge on SUV surface.

As for the safety, DOPG-SUV30 did not show a cell teratogenicity and VCAM-1 induction, which is a biomarker of cellular dysfunction triggered by LOX-1 signaling, indicating a low risk of safety for *in vivo* use.

In summary, the present study demonstrated that DOPG-SUV30 inhibits OxLDL/AcLDL binding to LOX-1 clusters on the cell surface, and can function as a DDS carrier targeting LOX-1 expressing pathological sites of atherosclerosis and cancer at least for *in vitro* use.

II-6. Figures and Tables

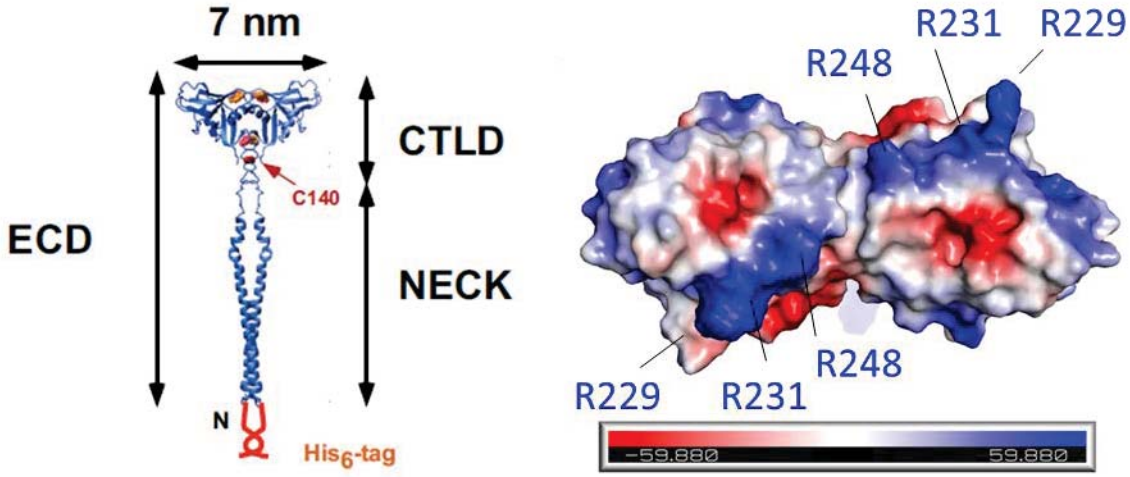

Fig. II-1.

Structure model for LOX-1 extracellular domain (ECD) (Left panel). The CTLD structure is the crystal structure (PDB code: 1YXK). The coiled-cold structure for the NECK domain is modeled based on the structure of myosin heavy chain. The LOX-1 ECD used in this SPR experiments harbors His_6-tag at its N-terminus for anchoring it to the sensor surface. Surface potential on LOX-1 CTLD dimer (Right panel). The positively charged sites are shown in blue, and the negatively charged sites are shown in red respectively. Arginine residues including R229, R231, and R248 form a belt of the basic residues on the flat surface of the CTLD dimer (Basic spine structure), which poses LOX-1 the preferential binding to the negatively charged ligands such as OxLDL. The image was produced using PyMOL v2.0.4 (Schrödinger, LLC).

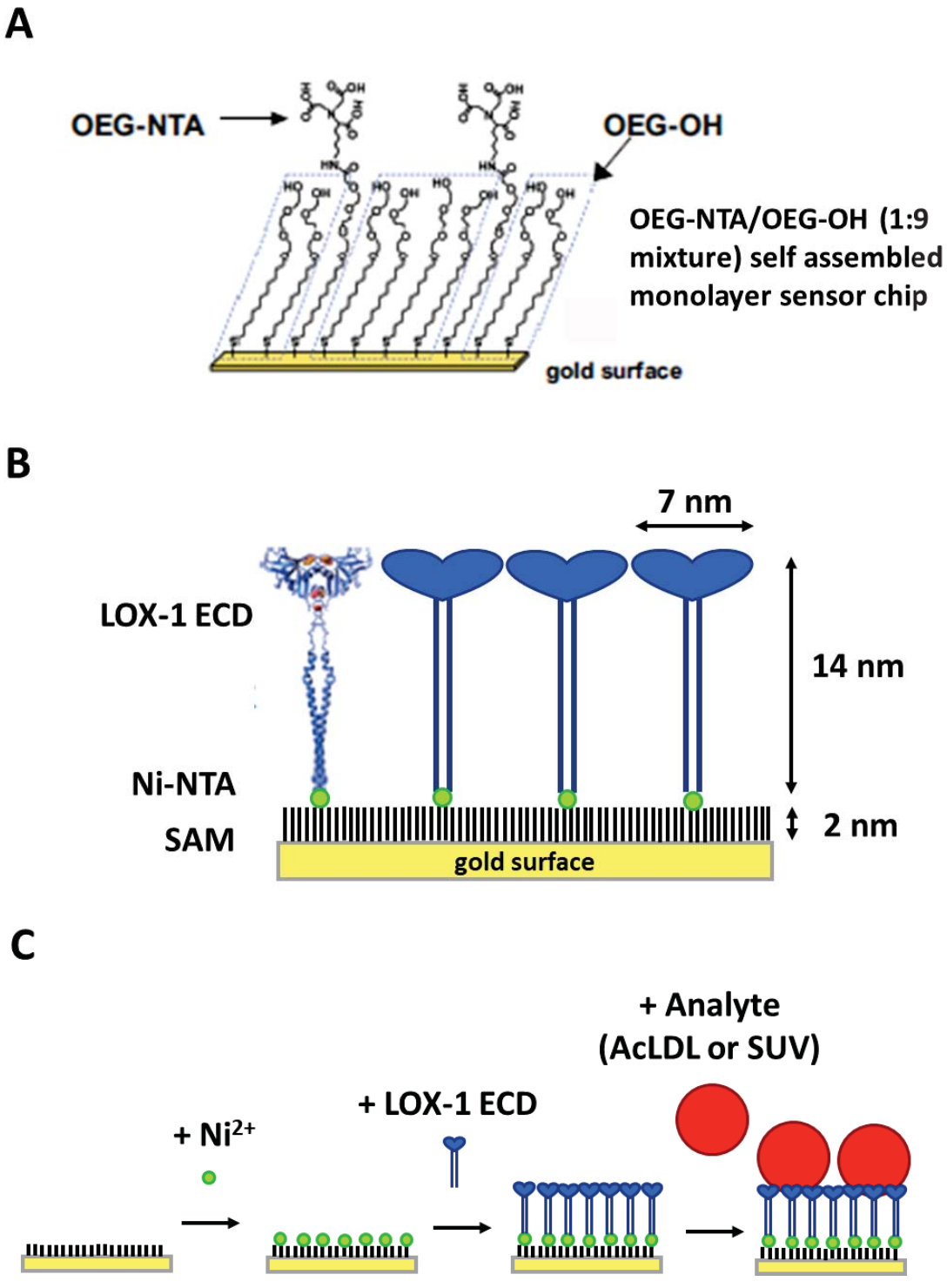

Fig. II-2.

Schematic diagram of the surface plasmon resonance (SPR) experiment used in this study.

(**A**) The chemical structure of the self-assembled monolayer (SAM) on the SPR sensor surface consists of 10% OEG-NTA and 90% OEG-OH. (**B**) Schematic drawing of the sensor surface doped with LOX-1 ECD via the His6-tag and Ni^{2+}-NTA interaction on the SAM. The figure is drawn by considering the relative sizes of the LOX-1 EXD and SAM (2 nm in thickness) with 10% OEG-NTA. (**C**) Injection workflow of this SPR experiment. LOX-1 ECDs were immobilized onto the Ni^{2+} loaded NTA-SAM sensor chip, and the affinity of AcLDL or DOPG/DOPC SUVs to LOX-1 clusters was measured.

A

DOPG: 1,2-Dioleoyl-*sn*-Glycero-3-[Phospho-*rac*-1-glycerol]

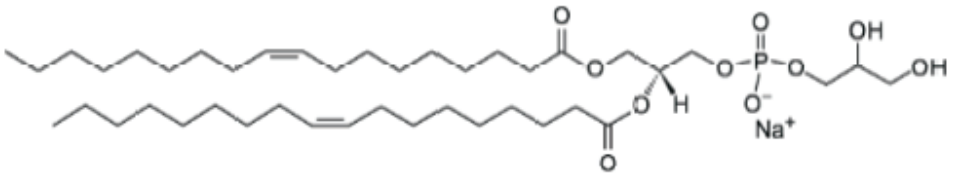

B

DOPC: 1,2-Dioleoyl-*sn*-Glycero-3-Phosphocholine

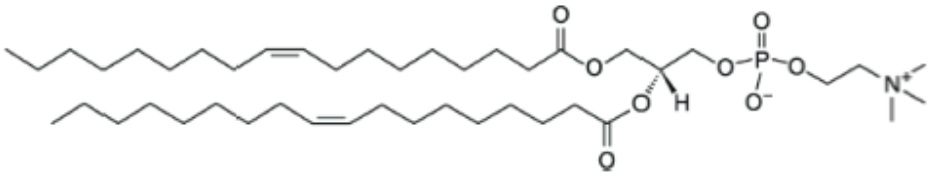

Fig. II-3.

Chemical structures for DOPG (**A**) and DOPC (**B**) used as raw materials for SUVs.

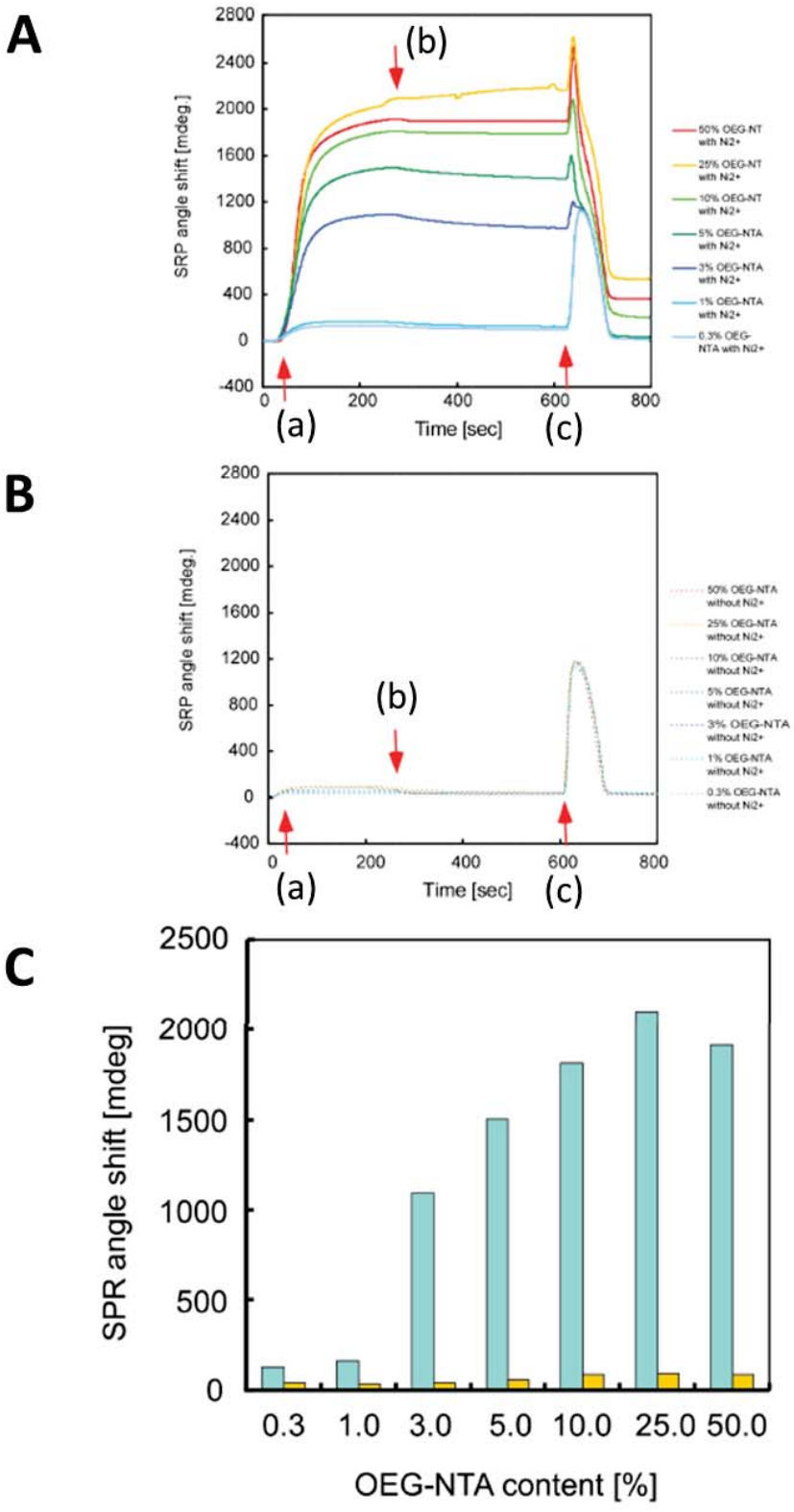
A
SRP angle shift [mdeg.]
Time [sec]
(a)
(b)
(c)
50% OEG-NT with Ni2+
25% OEG-NT with Ni2+
10% OEG-NT with Ni2+
5% OEG-NTA with Ni2+
3% OEG-NTA with Ni2+
1% OEG-NTA with Ni2+
0.3% OEG-NTA with Ni2+
B
SRP angle shift [mdeg.]
Time [sec]
(a)
(b)
(c)
50% OEG-NTA without Ni2+
25% OEG-NTA without Ni2+
10% OEG-NTA without Ni2+
5% OEG-NTA without Ni2+
3% OEG-NTA without Ni2+
1% OEG-NTA without Ni2+
0.3% OEG-NTA without Ni2+
C
SPR angle shift [mdeg]
OEG-NTA content [%]
0.3
1.0
3.0
5.0
10.0
25.0
50.0

Fig. II-4.

Optimization of SPR sensor responses for immobilizing LOX-1 ECD to SAM surfaces with different contents of OEG-NTA moieties with Ni loaded (**A**) and without Ni loading (**B**). The arrows indicate the times for switching the solutions flowing onto the sensor chip. The solutions contained (a) 0.1 mg/mL His_6-tagged LOX-1 ECD, (b) no solute and (c) 300 mM imidazole in 10 mM HEPES (pH 7.4) with 150 mM NaCl and 0.05 mM EDTA. (**C**) Comparison of the SPR sensor responses measured by the reflected light angle shifts at time point (b). Data from the sensor with Ni loaded to NTA (blue bars) and the corresponding data from the sensor without Ni loading (yellow bars). Data were collected with a SPR02 system (Optoquest Co.Ltd., Tokyo, Japan) at 25 °C.

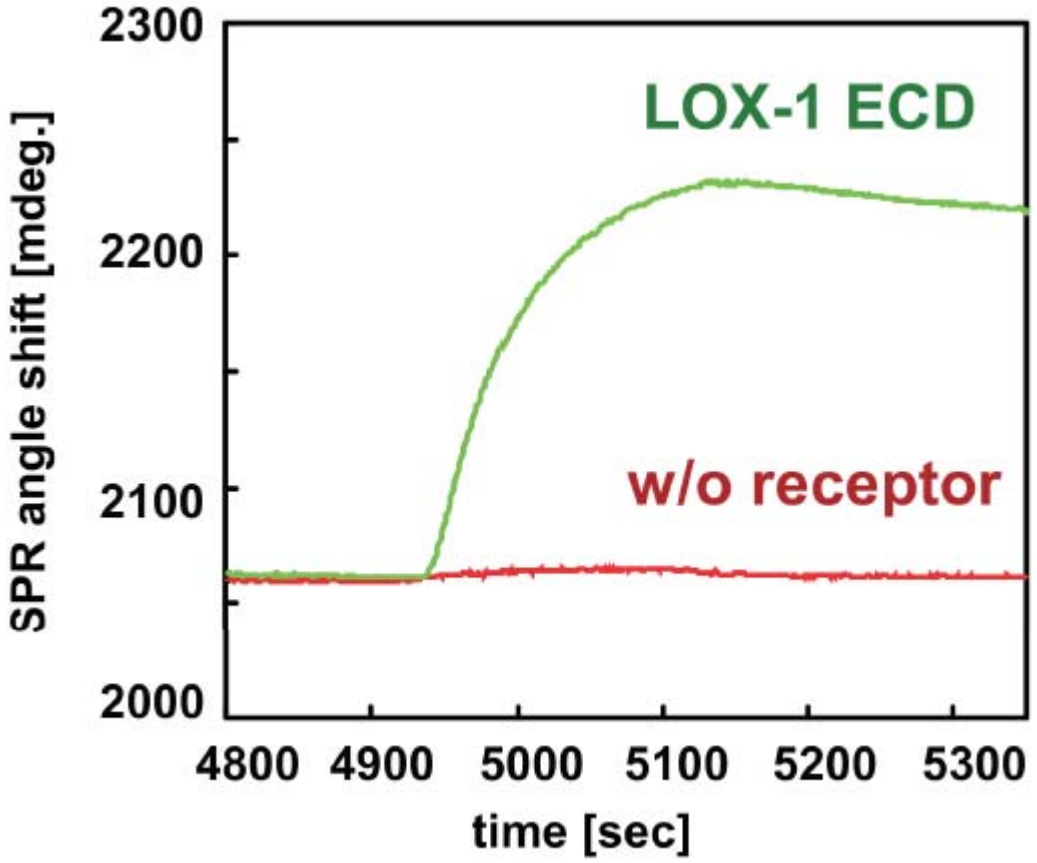

Fig. II-5.

The SPR sensorgrams for AcLDL binding to the sensor with LOX-1 ECD loaded onto the SAM (green) and the sensor coated with SAM but without LOX-1 ECD (red). The data were collected with a SPR02 system (Optoquest Co. Ltd., Tokyo, Japan) at 25 ℃.

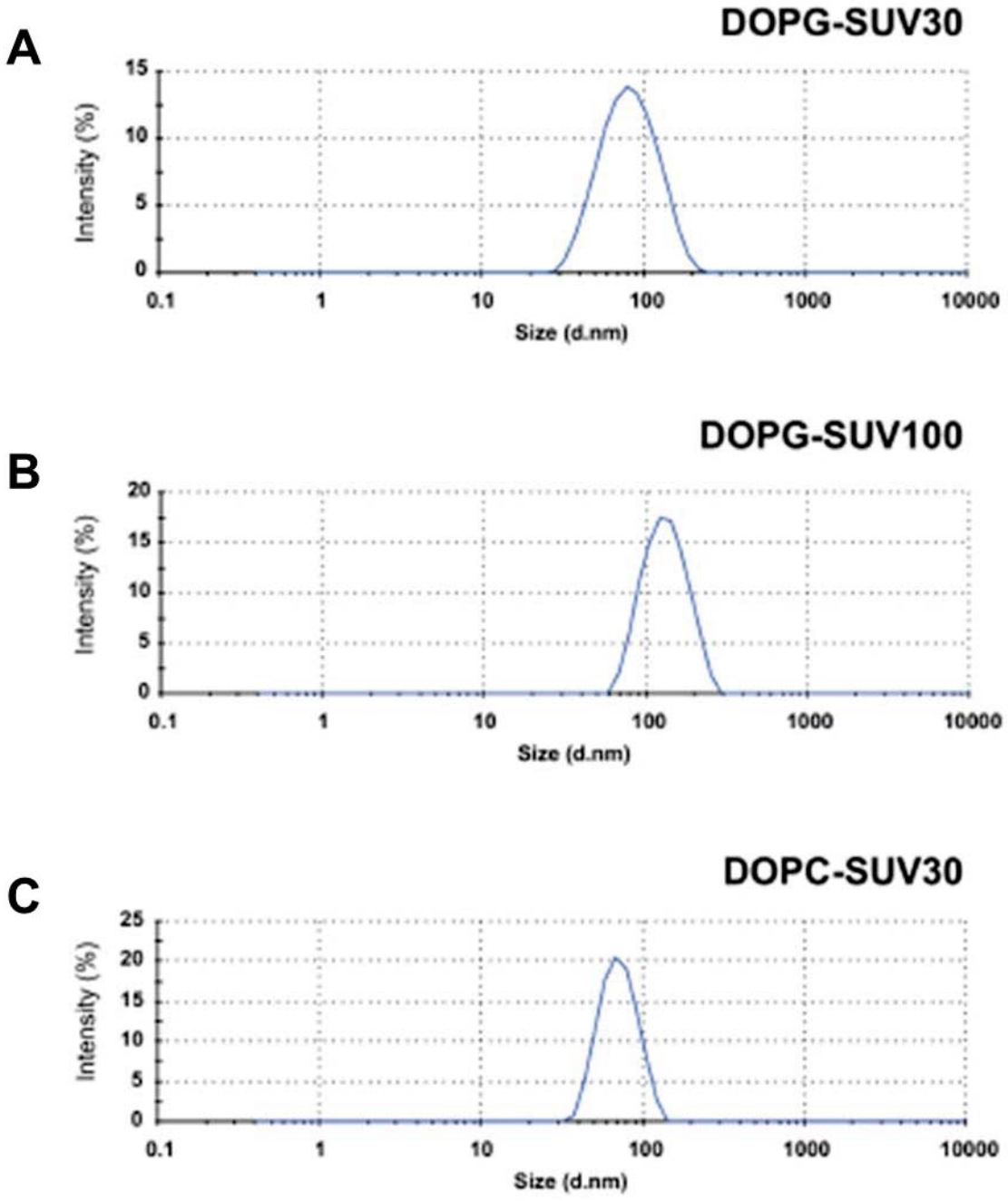

Fig. II-6.

The particle size (hydrodynamic diameter) distribution of DOPG-SUV30 (**A**), DOPG-SUV100 (B), and DOPC-SUV30 (**C**). All data were collected with a ZetaSizer Nano (Malvern Instruments Ltd., UK) at 25°C, which uses dynamic light scattering (DLS).

A

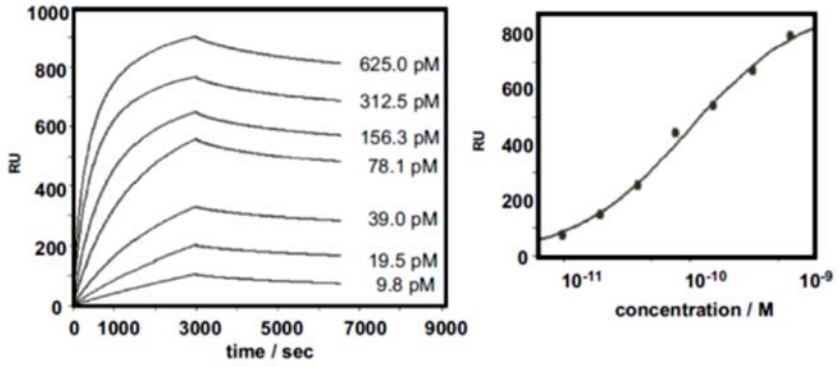
RU
time / sec
625.0 pM
312.5 pM
156.3 pM
78.1 pM
39.0 pM
19.5 pM
9.8 pM
concentration / M

B

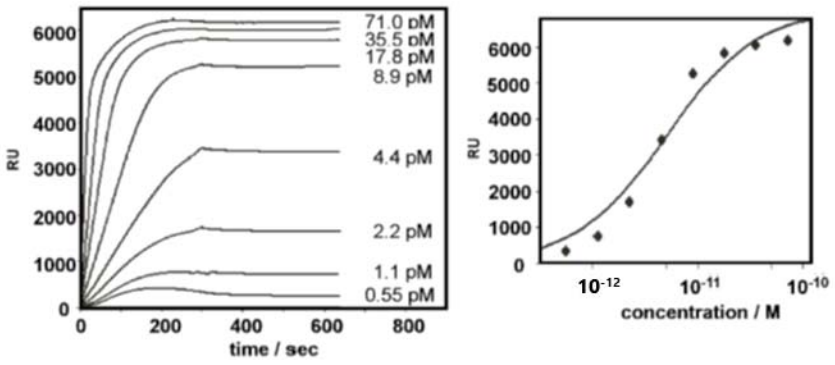
RU
time / sec
71.0 pM
35.5 pM
17.8 pM
8.9 pM
4.4 pM
2.2 pM
1.1 pM
0.55 pM
concentration / M

C

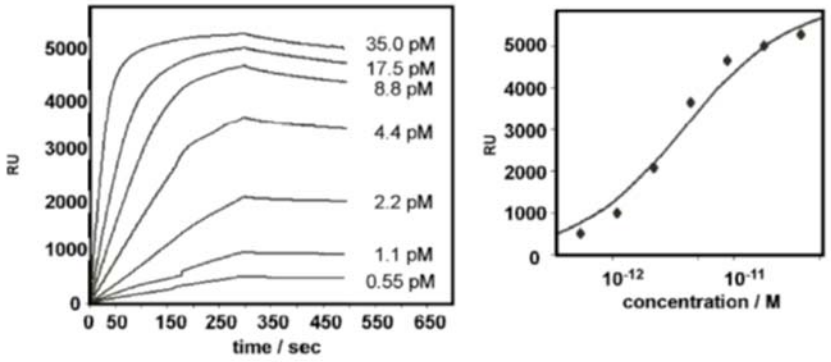
RU
time / sec
35.0 pM
17.5 pM
8.8 pM
4.4 pM
2.2 pM
1.1 pM
0.55 pM
concentration / M

D

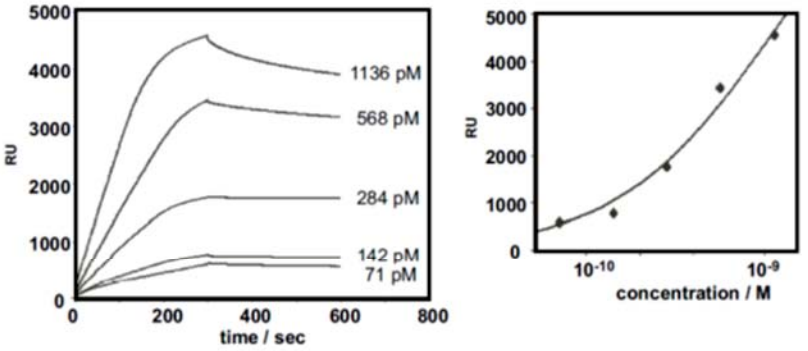
RU
time / sec
1136 pM
568 pM
284 pM
142 pM
71 pM
concentration / M

Fig. II-7.

SPR sensorgrams of each ligand binding to LOX-1 ECD clusters immobilized on SAM sensor chip. (**A**) AcLDL at concentrations of 9.8, 19.5, 39.0, 78.1, 156.3, 312.5 and 625.0 pM. (**B**) DOPG-SUV30 at concentrations of 0.55, 1.1, 2.2, 4.4, 8.8, 17.5 and 35.0 pM. (**C**) DOPG-SUV100 of the same concentration series as (B). (**D**) DOPC-SUV30 at concentrations of 71, 142, 284, 568, and 1136 pM.

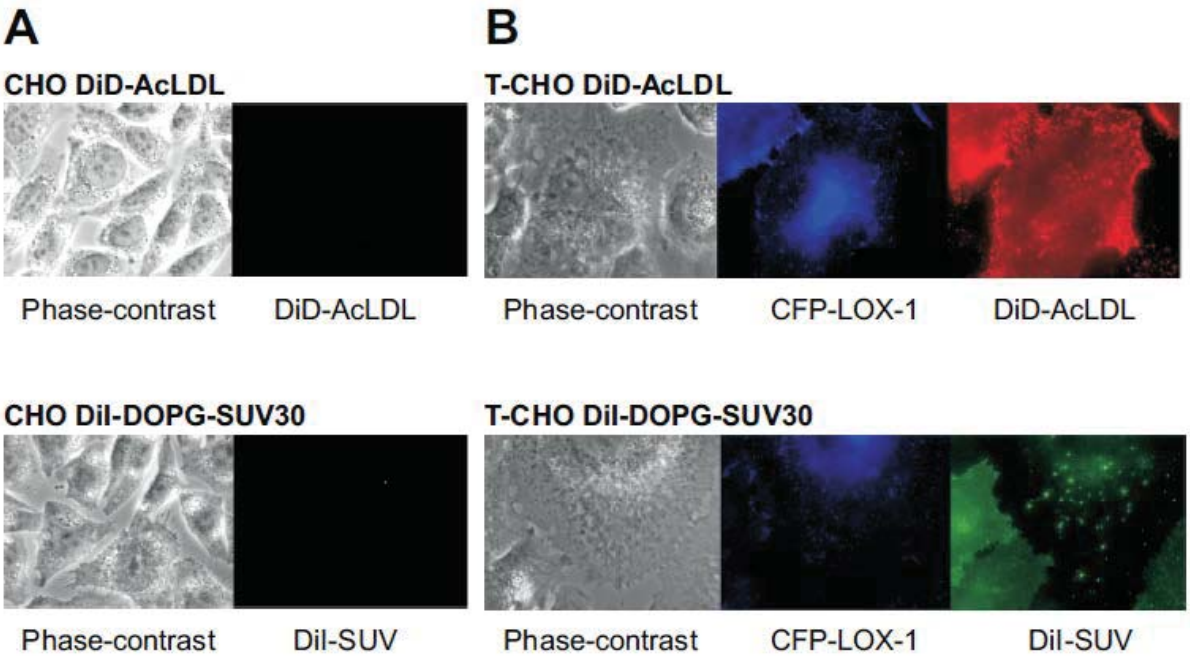

Fig. II-8.

Ligand uptake experiments using (**A**) native CHO cells and (**B**) CHO cells stably expressing CFP-fused LOX-1 (T-CHO). The data from native CHO cells contain phase contrast images (left) and fluorescence images (right) for DiD-AcLDL (excitation 620 nm) or DiI-DOPG-SUV30 (excitation 535 nm). The microscopic images from T-CHO cells are shown phase contrast images (left), the fluorescence images for CFP-LOX-1 (excitation 436 nm) (middle) and DiD-AcLDL (excitation 620 nm) or DiI-DOPG-SUV30 (excitation 535 nm) (right).

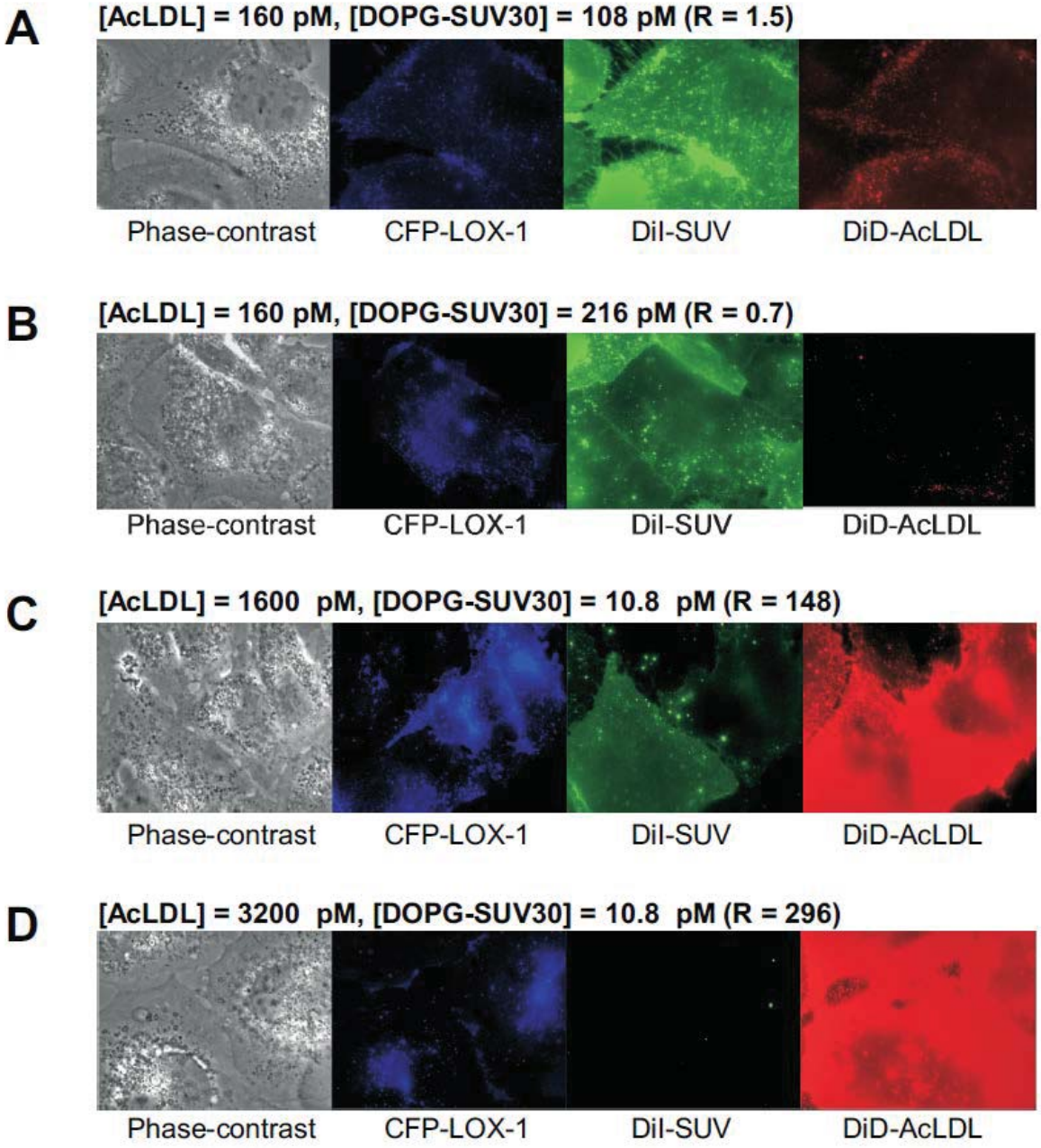

Fig. II-9.

Competitive uptake into T-CHO cells between DiI-DOPG-SUV30 and DiD-AcLDL. The amounts of DiD-AcLDL and DiI-DOPG-SUV30 were visually compared by fluorescence images for DiD-AcLDL (excitation 620 nm; red) and DiI-DOPG-SUV30 (excitation 535 nm; green) with monitoring of the CFP-LOX-1 expression by fluorescence images (excitation 436 nm; blue). The molar concentrations for the

input AcLDL and DOPG-SUV30 for each experiment are indicated in each set of images. R denotes the molar ratio defined as [DiD-AcLDL] / [DiI-DOPG-SUV30]. The molar ratios (Rs) for the input varied: (**A**) 1.5, (**B**) 0.7, (**C**) 148, and (**D**) 296. Each set of microscopic images includes the phase contrast cell images (left), and fluorescence images of CFP-LOX-1 (2nd left), DiI-DOPG-SUV30 (3rd left) and DiD-AcLDL (right).

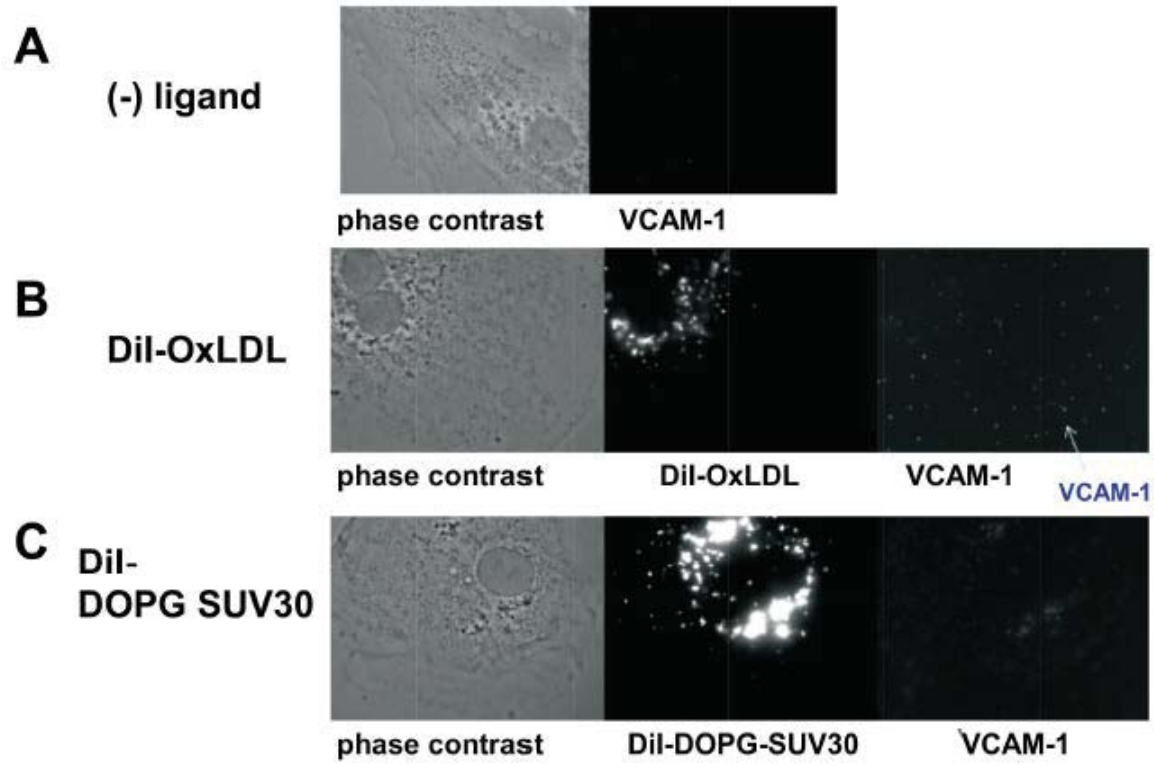

Fig. II-10.

VCAM-1 induction assay of DOPG-SUV30 against HAEC (human aortic endothelial cells). HAEC cultured without ligands did not express VCAM-1 (**A**). Phase contrast image of the cells (left) and the fluorescence image (excitation at 620 nm) stained with the anti-VCAM-1 antibody detected by the secondary antibody conjugated with Alexa Fluor 633 (right). The uptake of DiI-OxLDL into HAEC induced VCAM-1 on the surface (**B**). Phase contrast image (left), the fluorescence image for the internalized DiI-OxLDL (excitation at 535 nm) (middle) and the fluorescence image of detected VCAM-1 using the anti-VCAM-1 antibody (right). The representative spot detected on the cell is marked by an arrow. (**C**) HAEC internalized DiI-DOPG-SUV30 but did not induce VCAM-1. Phase contrast image (left), the fluorescence image of the internalized DiI-DOPG-SUV30 (middle) and the fluorescence image of cells stained with the anti-VCAM-1 antibody (right).

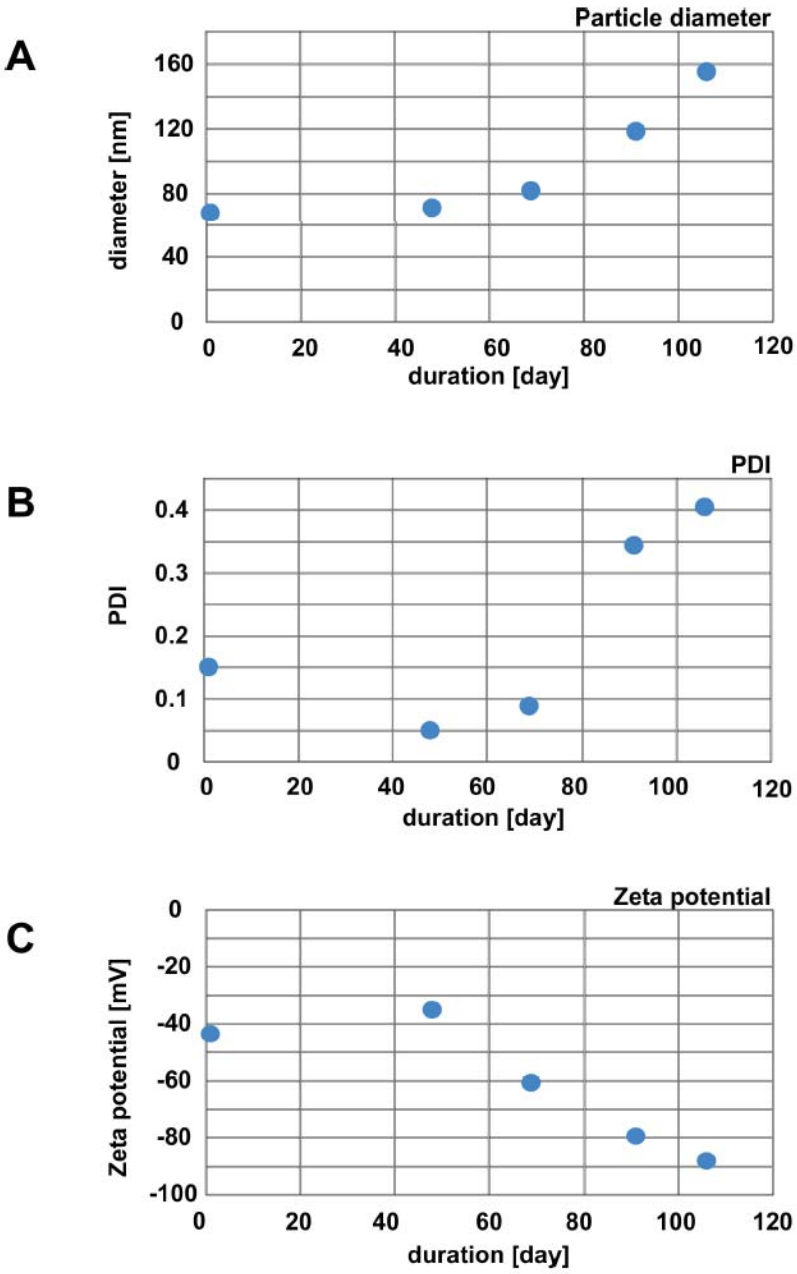

Fig. II-11.

The physicochemical stability of the DOPG-SUV30 during storage in water at 25 °C. (**A**) The hydrodynamic diameter, (**B**) the polydispersity index, and (**C**) the zeta potential. Data were collected with a ZetaSizer Nano system (Malvern Instruments Inc., UK) at the time points of 1, 47, 71, 93 and 109 days after preparation.

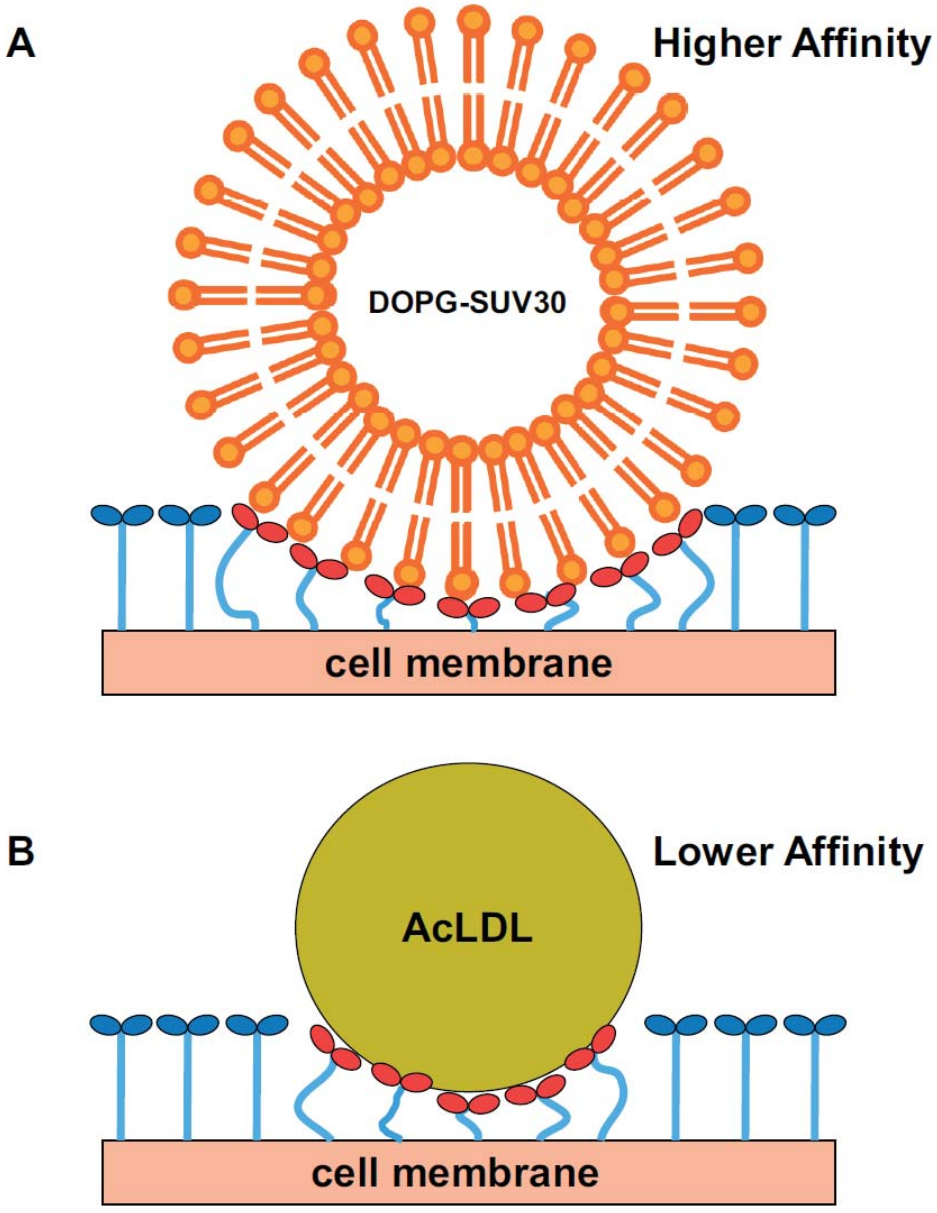

Fig. II-12.

Schematic images showing the interaction of the LOX-1 ECDs-SAM sensor with DOPG-SUV30 (**A**) and AcLDL (**B**). The diameters of DOPG-SUV30 (70 nm) and AcLDL (38 nm), and the molecular size of LOX-1 ECD are considered in the drawings. The CTLDs of LOX-1 in direct contact with the vesicle are shown in red.

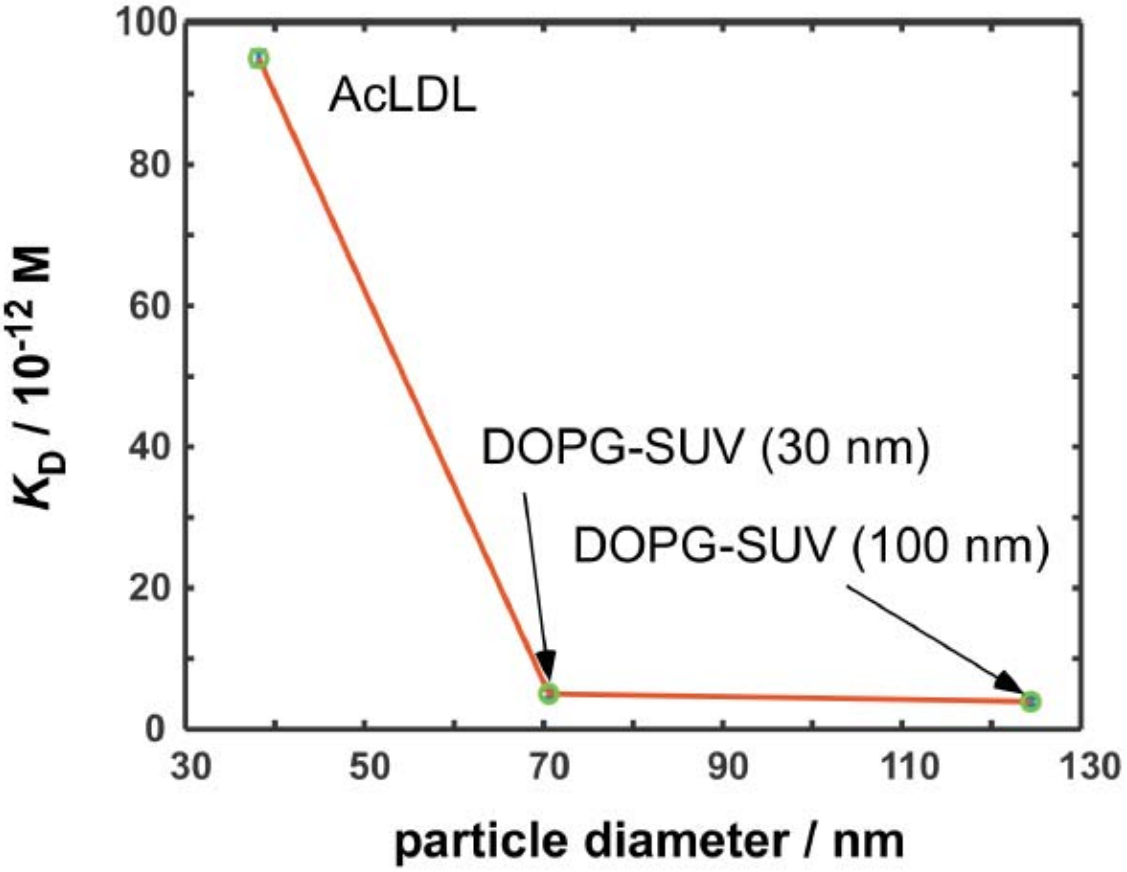

Fig. II-13.

The size dependency of the affinities of the negatively charged vesicles toward the LOX-1 ECD-SAM sensor.

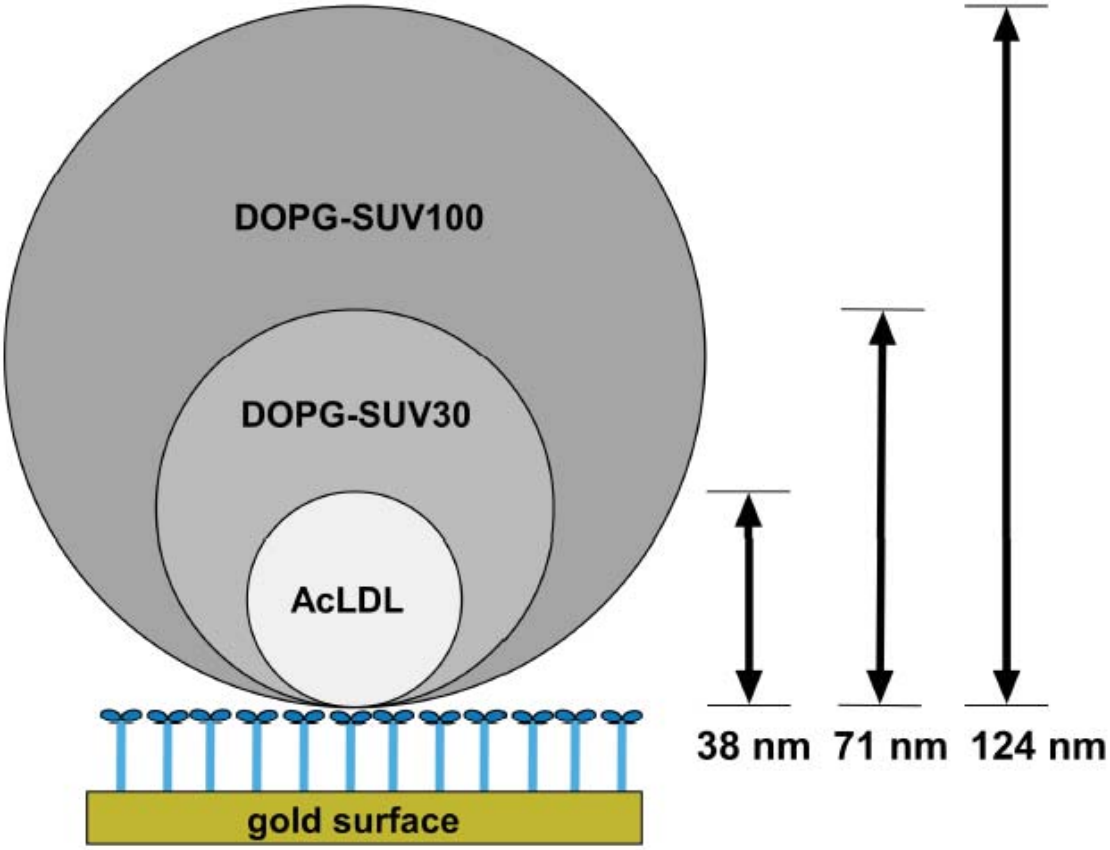

Fig. II-14.

Comparison of the sizes of DOPG-SUVs and AcLDL. The drawings consider the relative sizes of the vesicles to LOX-1 ECD.

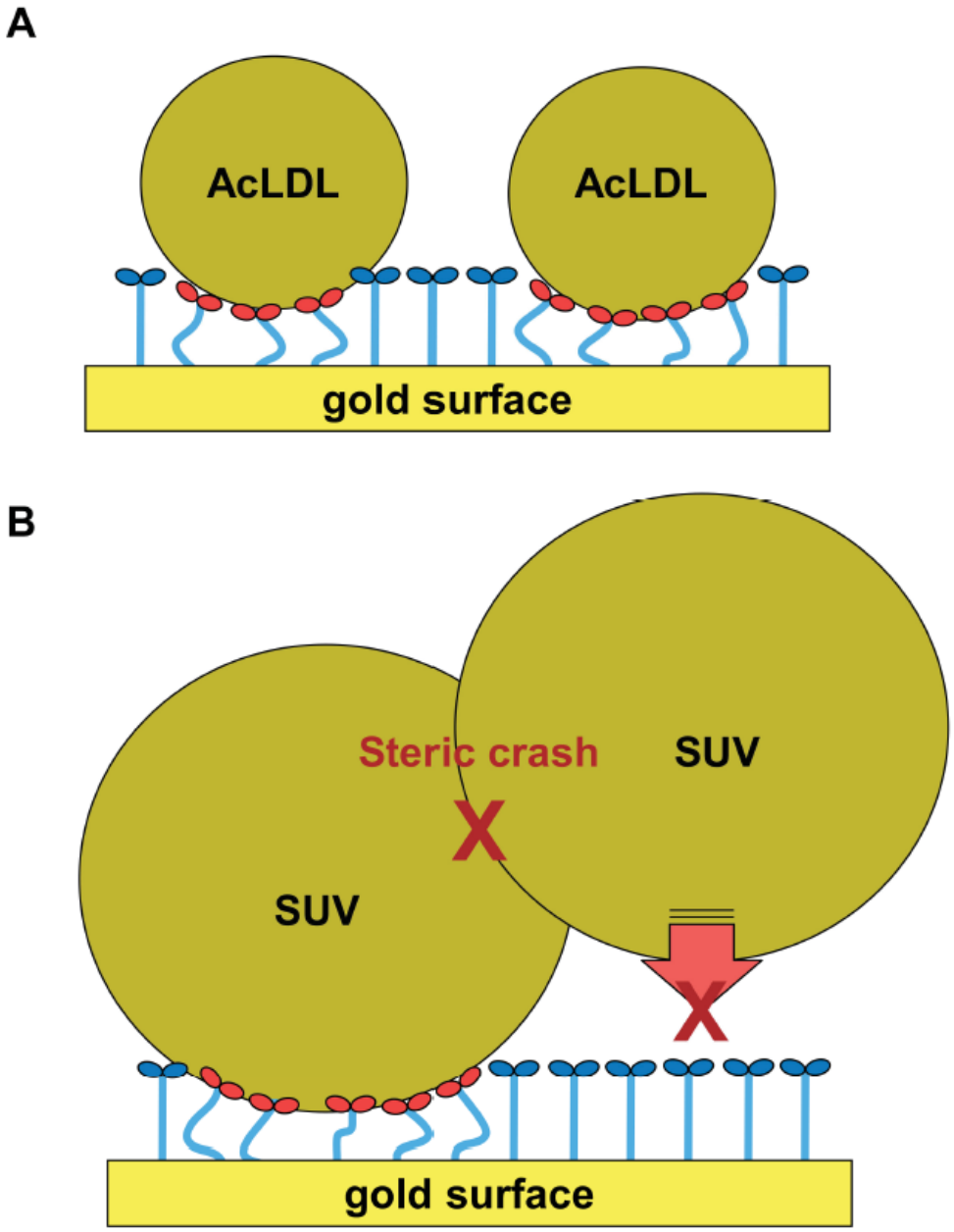

Fig. II-15.

Schematic images describing the steric clash among vesicles on the LOX-1 ECD-SAM sensor surface. Smaller vesicles (**A**) bind to the surface more than larger vesicles (**B**). On the limited surface of the SPR sensor, the total number of bound vesicles will be reduced because of steric clashes that prohibit the interaction of additional vesicles with the surface.

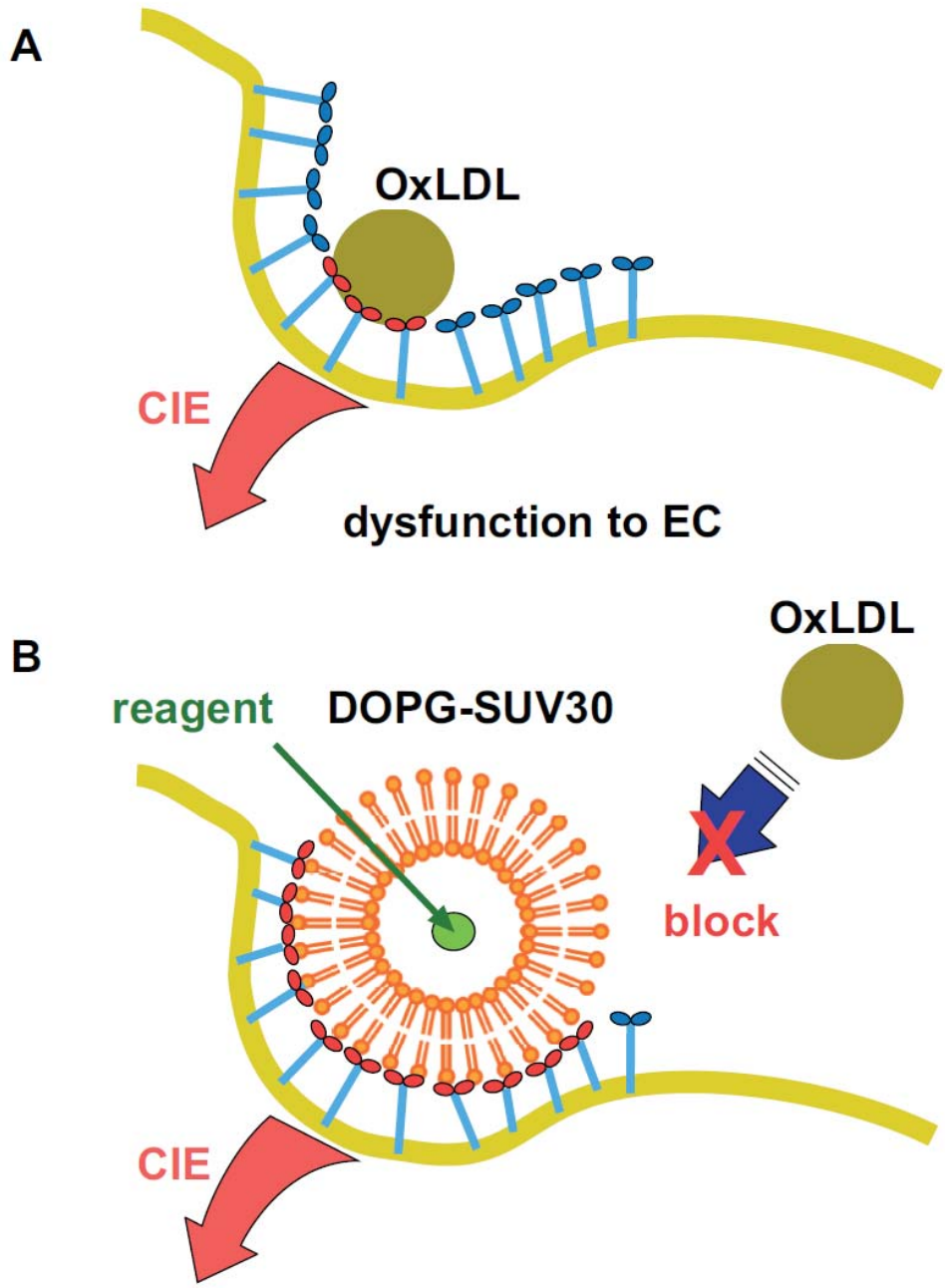

Fig. II-16.

Schematic drawings of the interactions of OxLDL (**A**) and DOPG-SUV30 (**B**) with LOX-1 clusters at the clathrin-independent endocytosis (CIE) entry site to be internalized into the cell. The drawings consider the plausible size for the CIE entry site, and also the sizes of OxLDL (23 nm in diameter), DOPG-SUV30 and LOX-1 ECD.

Table. II-1

List of hydrodynamic diameters, zeta potentials and dissociation constants (K_D) with LOX-1 ECD clusters for AcLDL and each SUV

Ligand	Hydrodynamic diameter (nm)	Zeta potential (mV)	K_D ($\times 10^{-12}$ M)
AcLDL	38.2 ± 0.5	-41.0 ± 2.1	95 ± 1
DOPG-SUV30	70.6 ± 0.2	-42.2 ± 0.2	5.0 ± 0.7
DOPG-SUV100	124 ± 0.4	-41.6 ± 2.1	3.9 ± 0.5
DOPC-SUV30	68.2 ± 0.1	-8.4 ± 0.4	1300 ± 100

Chapter III The role of disulfide bond in CDR-H3 of chicken-derived anti-LOX-1 monoclonal antibody HUC52 for the antigen recognition

III-1. Introduction

A number of studies using mouse-derived anti-LOX-1 mAbs, for example, named TS92 (aka JTX92) [8,36,82–84], JTX-20 [11,85] and #10-1 [86], have been reported to date. Those mAbs inhibited LOX-1 signaling pathways, and improved the pathology progressions effectively [6,36,83,87,88]. These results demonstrate that anti-LOX-1 mAbs are promising therapeutic or diagnostic agents for LOX-1 targeting therapy.

A chicken-derived anti-LOX-1 mAb named HUC52 has been generated by Iwamoto *et al.* [42]. Since chickens are phylogenetically distant from mammals, when antigens are highly conserved between humans and mice, it is used as an immune host animal which has the possibility to produce antibodies that can't be produced in mammals [89]. In fact, HUC52 binds to human LOX-1 CTLD strongly, and inhibits uptake of OxLDL. It cross-reacts with human, pig and rabbit LOX-1 orthologs, but does not bind to mouse LOX-1. It has two cysteine residues capable of forming a disulfide bond in the third complementarity-determining region of heavy chain (CDR-H3) [90], which should be the center of antigen binding [91]. Disulfide bridged complementarity determining regions (CDRs) are often found in chicken antibodies [92,93], and thought to be important for antigen binding. On the other hand, those are rarely seen in mouse or human-derived mAbs [94]. This is a unique feature of chicken antibodies, but there are only a few studies that elucidated precisely the structure and epitope recognition mechanisms of disulfide-bridged CDRs [93].

In this chapter, I analogized that HUC52 would have a characteristic CDR-H3 structure constrained by a disulfide. To understand what structure CDRs of HUC52 shape and how they interact with CTLD dimer is an important research topic for considering antibody biology and development of LOX-1 targeting biopharmaceuticals. Based on these backgrounds, computer simulation studies were conducted to construct the three-dimensional (3D) structure models of HUC52 fragment antigen-binding (Fab) domain and its complex with LOX-1 CTLD dimer in order to estimate their interaction mechanism. For each HUC52 Fabs with and without disulfide bond in CDR-H3, their binding manners to LOX-1 CTLD were compared. The mechanism for the cross-reactivity of HUC52 to LOX-1 orthologs was also investigated from the simulated model.

III-2. Materials and methods

III-2-1. Amino acid sequence information

Sequences of three CDRs of heavy chain of HUC52, i.e. CDR-H1, CDR-H2 and CDR-H3, were obtained from published patent information (WO/2010/147171A1) [90] (Table. III-1).

All sequences of HUC52 were not disclosed except for the heavy chain CDRs. Therefore, sequences of heavy chain (VH-CH1) and light chain (VL-CL) of a chicken-human chimeric IgG1λ Fab (Protein Data Bank (PDB) code: 4GLR) [93], which was obtained by fusing variable region of a chicken-derived antibody binding to phosphorylated peptide of Tau protein and constant region of human IgG1λ, was used as template (Table. III-S1). Heavy chain CDRs of template and those of HUC52 were replaced to generate HUC52 Fab model.

III-2-2. Construction of HUC52 Fab structure model

An initial 3D structural model of HUC52 Fab was generated by using Phyre2 server system [95] under intensive modeling mode. Since only single sequence could be input in the system, a Fab heavy chain (VH-CH1) model alone was obtained at first. PyMol Molecular Graphics System, Version 2.0 (Schrödinger, LLC) (PyMOL) was used for graphicization of those models. Then, the coordinate of initial Fab heavy chain model and that of template Fab crystal structure were superimposed with an align function of PyMOL. It was fitted for C_α atoms of both molecules. Finally, a coordinate of virtual Fab consisting of the heavy chain having CDRs of HUC52 and the light chain of template was generated by removing the template heavy chain from the superimposed coordinates (HUC52 Fab). This model was refined by ModRefiner [96]. This was further processed to patch disulfide bonds explicitly between $C99^H$ and $C107^H$ in CDR-H3, $C22^H$ and $C96^H$ in VH, $C152^H$ and $C208^H$ in CH1, $C23^L$ and $C89^L$ in VL, $C138^L$ and $C197^L$ in CL and refined the overall structure additionally by using MODELLER software version 9.20 [97] (Hereafter, amino acid residues of CTLD A-chain, B-chain, and HUC52 Fab heavy chain and light chain are designated by the superscript chain identifiers A, B, H, and L, respectively). Five models were generated, and confirmed that all models are almost the same. Therefore, the lowest DOPE score [98] model (-42218 points) was regarded as a representative structure of HUC52 Fab with disulfide bond in CDR-H3.

In order to compare the effect of absence of disulfide in the CDR-H3, another 3D model of HUC52 Fab without the disulfide bond was also generated by MODELLER. The coordinate refined by ModRefiner was processed additionally by explicitly patching disulfide bonds on the four sites other than $C99^H$-$C107^H$ in the CDR-H3. Five models were generated in the same way as above, and the lowest DOPE score model (-42186 points) was subjected subsequently to loop modeling only for the region of CDR-H3 to generate 100 models. Among these, a model with no steric hindrance and the lowest DOPE score (-1856 points) was taken as a representative structure of HUC52 Fab without disulfide bond in CDR-H3. Hydrogen atoms were loaded into both models finally.

III-2-3. Docking simulation of HUC52 Fab and CTLD dimer

Docking simulation was conducted by using ZDOCK version 3.0.2 [99,100]. Coordinate of X-ray crystal structure of human LOX-1 CTLD dimer (PDB code: 1YXK) [16] was used, and hydrogen atoms were loaded on PyMOL. Coordinates of HUC52 Fab with or without disulfide in CDR-H3 generated by MODELLER were used as ligands. In addition, template Fab was also used as a negative control ligand. In simulation condition setting, Non-CDR regions of Fabs were excluded from antigen binding site since control IgG did not react with LOX-1 in the previous study [42]. In addition, CDRs of light chain were also excluded since these were derived from template. The qualities of local structures of each complex model were checked using the Fine Packing Quality Control module [101] of WHAT IF server [102]. There were no residues judged wrong.

III-3. Results

III-3-1. Structural models of HUC52 Fab

Two virtual Fab models having CDRs of HUC52 heavy chain were generated by *in silico* approach. One forms a disulfide bond in the CDR-H3 (Fab with disulfide) and the other doesn't form it (Fab without disulfide). In case of Fab with disulfide, the CDR-H3 shaped a β hairpin like loop (Fig. III-1 A). A χ3 dihedral angle of the disulfide formed in CDR-H3 was 153.125 degree. On the other hand, The CDR-H3 without disulfide lost β hairpin structure, and instead shaped a random coil-like region (Fig. III-1 B). From observations of the models generated by loop modelling, there is a high possibility that CDR-H3 without disulfide is fluctuating randomly without shaping a specific structure. These results suggest that the disulfide bond constrain CDR-H3 loop to a specific conformation. Only in CDR-H3 with disulfide, the side chain of $Y105^{H}$ protruded to the antigen side (outer side). The orientation of $Y101^{H}$ also changed (Fig. III-1 C).

III-3-2. Effect of the disulfide bond in CDR-H3 for antigen binding

III-3-2-1. Evaluation of complex models by ZDOCK scores

As a result of docking simulation by ZDOCK program, 2000 decoys were calculated for each Fab-CTLD complex. A higher ZDOCK score means that the charge and shape complementarity between the Fab and CTLD dimer in the complex model is better [103]. Distributions of ZDOCK scores for all decoys were plotted in Fig. III-2. The 1^{st} ranked model of HUC52 Fab with disulfide and CTLD dimer complex resulted in the highest ZDOCK score (1189.735 points) among all models compared. In case of HUC52 Fab without disulfide, ZDOCK score of the 1^{st} ranked complex model was 1047.274 points at most. In case of template Fab used as a negative control, the highest ZDOCK score was 823.626 points.

III-3-2-2. Comparison of binding positions of each Fab on CTLD dimer

Spatial distributions of center of mass of each Fab ligand binding to CTLD dimer with the top 100 ZDOCK scores were plotted in Fig. III-3. Fabs bound to OxLDL interface on CTLD in the majority of complex models. A clear trend difference was not found among Fab ligands for the binding positions. Template Fabs also bound predominantly to OxLDL interface on CTLD. However, template Fab and HUC52 Fab without disulfide were found to be distributed more on the opposite side of OxLDL interface of CTLD than one with disulfide. In order to compare this with numerical values, the number of basic spine arginine (Arg) residues on CTLD dimer (R208, R229, R231, and R248) that interacted with each Fab was counted for the complex models up to the top 20 ZDOCK score ranks. An average of 1.95 Arg residues interacted with HUC52 Fab with disulfide. On the other hand, an average of 1.35 Arg residues interacted with Fab without disulfide. In case of template Fab, an average of 1.40 Arg residues bound to it. Thus, HUC52 with disulfide tended to contact with more Arg residues of basic spine than the others.

III-3-3. Interaction mechanism between HUC52 Fab and CTLD dimer

The 1st ranked complex model in ZDOCK score (1189.735 points) were regarded as a representative result of the docking simulation using HUC52 Fab with disulfide (Fig. III-4), and details of its interaction mechanism were analyzed. The correlation diagrams for interaction between epitopes and paratopes are shown in Fig. III-5 A. Looking at the number of interactions in the complex model, 4 hydrogen bonds and 308 non-bonding atomic contacts were found between the Fab and CTLD dimer (Table. III-2).

Identified interaction sites were mapped on 3D structural model (Fig. III-6). For this complex model, 25 residues of Q192^{A}, I195^{A}, S196^{A}, Y197^{A}, S198^{A}, S199^{A}, F200^{A}, P201^{A}, R231^{A}, G232^{A}, A233^{A}, Y245^{A}, Q247^{A}, R248^{A}, Y252^{A}, A253^{A}, E254^{A}, L258^{A}, A259^{A}, A260^{A} of CTLD A-chain, S160^{B}, G161^{B}, S162^{B}, F200^{B}, and F261^{B} of CTLD B-chain were found as candidate epitopes (Fig. III-6 A). For HUC52 Fab, 13 residues of S52^{H}, T54^{H}, G55^{H}, S56^{H}, Y57^{H} belonging to CDR-H2, Y101^{H}, S102^{H}, S103^{H}, G104^{H}, Y105^{H}, D106^{H} belonging to CDR-H3, D31^{H} of CDR-H1 and R72^{H} of framework region were estimated as candidate paratopes (Fig. III-6 B). Four hydrogen bonds were formed between S52^{H} and Y245^{A}, Y101^{H} and S199^{A}, S103^{H} and S198^{A}, Y105^{H} and S160^{B}. Atomic contacts by hydrophobic interaction were observed in regions of Y101^{H}-D106^{H}, T54^{H}-Y57^{H}, R72^{H}, and D31^{H} of HUC52 with their corresponding epitopes. Y105^{H} contacted with the area formed by S160^{B}-S162^{B} and F261^{B} (Fig. III-6 C). Y101^{H} interacted so as to enter into space among S199^{A}, Q247^{A} and R248^{A}. S103^{H} and G104^{H} interacted with their epitopes (Q192^{A}, S196^{A}, S198^{A}, etc.) so that the tip of CDR-H3 entered into the bottom area of groove at boundary between CTLD A-chain and B-chain. Y57^{H} contacted extensively with the epitopes (R231^{A}, G232^{A} and Y252^{A} etc.). D31^{H} and S102^{H} contacted to F200^{A} and F200^{B} respectively. Contacts of D106^{H} and R72^{H} to CTLD were very small, and their contribution would be limited.

Docking simulation for CTLD dimer and HUC52 Fab without disulfide resulted in a decoy complex model

of 1047.274 points with the highest score. The complex model is shown in Fig. III-7. Fab without disulfide also bound to OxLDL interface on CTLD (Fig. III-7 A), but its position and correspondence between epitopes and paratopes were quite different from those of Fab with disulfide above. Eight hydrogen bonds and 368 non-bonded contacts were found (Table. III-2). As shown in Fig. III-7 B, the side chains of $Y101^{H}$ and $Y105^{H}$ faced the opposite side of CTLD. Especially interactions between $Y105^{H}$ and CTLD were lost completely. Instead, $C99^{H}$, $A100^{H}$, $C107^{H}$, and $D108^{H}$, which were not involved in antigen recognition in case of Fab with disulfide, bound to CTLD (Fig. III-5 B).

III-4. Discussion

III-4-1. Validity of HUC52 Fab structural model

HUC52 Fab 3D models calculated from this simulation study were constructed from the sequences of heavy chain CDRs of HUC52 and template chicken-human chimeric Fab, because it has been reported that framework regions in Fv domain are generally well preserved among chicken derived antibodies [92].

In the HUC52 Fab with disulfide model, the CDR-H3 shaped a β hairpin like structure by being constrained with disulfide bond between $C99^{H}$ and $C107^{H}$. As an important biological property found in chicken antibodies, about >50% of clones tend to include cysteine residues in their CDRs, and they are likely to form disulfide bonds preferentially [92]. The importance of disulfide in CDR-H3 for antigen binding has already been demonstrated in several previous studies. For example, X-ray crystal structure of chicken-derived anti-phosphorylated Tau peptide mAb [93], which is used as a template Fab in this study, has revealed that the CDR-H3 constrained by disulfide shapes a characteristic compact conformation and presents binding sites for the antigen peptide. Another previous study using anti-human cytokine human mAb named M3 having a disulfide bond in the CDR-H3 has also reported that the disulfide was essential for antigen binding by biochemical experiments using alanine substituted mutants and molecular dynamics (MD) simulation [94]. The MD simulation has demonstrated that M3 CDR-H3 lacking the disulfide had changed the conformation and motility compared with one forming disulfide. From these findings, I analogize that HUC52 should form the disulfide bond in the CDR-H3 and contribute to the antigen binding.

In case of the Fab without disulfide lost the β hairpin CDR-H3 structure, and instead shaped a random coil-like region (Fig. III-1 B). The CDR-H3 without disulfide would be fluctuating randomly without shaping a specific structure. These results suggest that the disulfide bond constrain CDR-H3 loop to a specific conformation. As a result of docking simulation with CTLD dimer using the HUC52 Fab without disulfide, the interaction of $Y105^{H}$ in CDR-H3 with the epitopes was abolished, and that of $Y101^{H}$ was also greatly attenuated. However, surprisingly, the total number of hydrogen bonds and atomic contacts formed was larger than that of Fab with disulfide (Table III-2). Since the shapes of CDR-H1 and H2 are the same in both Fab models, therefore

their interactions should be maintained in both models. This docking simulation result derived from Fab without disulfide might contain overestimated errors due to the roughness of the prediction accuracy of ZDOCK program.

Assuming that HUC52 does not form the disulfide bond in CDR-H3, it cannot be rationally explained why HUC52 had to have two cysteine residues in the CDR-H3, and why HUC52 has been screened as a high affinity anti-LOX-1 mAb among countless clone repertoire. If the disulfide bond was not necessary, mAb clones in which $C99^{H}$ and $C107^{H}$ were substituted by other amino acid residues could be screened as anti-LOX-1 mAb. However, such clones were not found in the disclosed patent information [90], or in the previous study that created anti-LOX-1 mAbs from chickens by Iwamoto *et al* [42]. It would more reasonable to think that a chicken's immune system incorporated the two cysteines into there because the disulfide bond at that position in CDR-H3 of HUC52 was required for LOX-1 CTLD recognition. Therefore the real HUC52 should form the disulfide bond in CDR-H3.

III-4-2. Inhibition mechanism of OxLDL uptake of CTLD by HUC52

HUC52 Fabs bound to the center of OxLDL binding interface on CTLD in the majority of complex models despite not restricting anything for the binding site on CTLD in ZDOCK simulation set up (Fig. III-3). The Fab-CTLD dimer complex model (Fig. III-4) can explain simply the mechanism that HUC52 binds to OxLDL binding surface on CTLD dimer and inhibits OxLDL access by masking it physically. This is consistent with the fact that basic spine arginine residues on CTLD are required for OxLDL binding.

On the other hand, it is unlikely that HUC52 accesses to the periphery of hydrophobic tunnel penetrating CTLD dimer, which is thought to be a binding site for various small molecule LOX-1 inhibitors [56,104,105]. Thakkar *et al.* have found two small molecule synthetic compounds as LOX-1 inhibitor by virtual screening technique [41,49]. Both compounds named Mol-4 and Mol-5 entered the hydrophobic tunnel and interacted with side chains of Y197 and F158 which is exposed in it. As another example, Falconi *et al.* have developed a modified phospholipid, named PLAzPC as LOX-1 inhibitor [40]. Docking simulation indicated that PLAzPC also fills the hydrophobic tunnel of CTLD, in addition, side chains of $Q193^{A}$, $S198^{A}$ and $S160^{B}$ located around edges of the tunnel interact with hydrophilic PLAzPC spots. The main chain oxygen atoms of $S198^{A}$ and $S160^{B}$ formed hydrogen bonds with CDR-H3 of HUC52 with disulfide in this study (Fig. III-6 C). This partial similarity and contrasts for their interaction manners with CTLD found in these synthetic compounds and HUC52 Fab are interesting for considering the difference between their LOX-1 inhibition mechanisms.

III-4-3. Mechanism that HUC52 distinguishes LOX-1 orthologs

III-4-3-1. Relationship between the amino acid residues conserved among LOX-1 orthologs and the HUC52 interaction sites

In order to characterize the cross-reactivity of HUC52 to LOX-1 orthologs, the binding activities to LOX-1 orthologs from different animal species (human, pig, rabbit, and mouse) have been evaluated by biochemical experiments in previous study [42]. It has resulted in that HUC52 strongly bound to human, pig and rabbit LOX-1, but did not bind to mouse LOX-1. Based on this experimental fact, I examined whether this simulated complex model can explain the cross-reactivity mechanism of HUC52 to LOX-1 orthologs. If the model could explain logically how HUC52 distinguishes LOX-1 orthologs, it would be the evidence that the model reflects the real antigen-antibody interaction and is a credible one.

Sequence alignment of LOX-1 orthologs derived from human, pig, rabbit and mouse was analyzed using Clustal X [106]. The relationship between epitopes identified from ZDOCK simulation and conservativeness among LOX-1 orthologs is shown in Fig. III-8. Among them, 7 residues (S160, Q192, S198, S199, F200, A233 and R248) of human LOX-1 CTLD emerged as epitopes not conserved only in mice. As described in results section, these residues except A233 were important epitopes forming hydrogen bonds or close hydrophobic interactions with HUC52 with disulfide bonded CDR-H3 (Fig. III-5 A). A233 of human LOX-1 is converted to a valine in only mouse LOX-1, however, its contact with HUC52 was slight. This amino acid substitution in mouse CTLD might block the contact of HUC52 to around of the valine residue physically because valine side chain is bulky than that of alanine. This HUC52 Fab-CTLD dimer complex model could explain logically the cross-reactivity of HUC52 to LOX-1 orthologs.

III-4-3-2. Comparison of another anti-LOX-1 mAb HUC5-9 and HUC52

In the previous study that has generated anti-LOX-1 mAbs from chickens by Iwamoto *et al* [42], several anti-LOX-1 mAb clones have also been isolated besides HUC52. One of them, HUC5-9 had CDR-H1 identical to HUC52 and CDR-H2 and CDR-H3 partially similar to HUC52, but was different from HUC52 in that it could not bind to rabbit LOX-1. Focusing on the differences between HUC5-9 and HUC52, we will further discuss the validity of this Fab-CTLD complex model.

Comparison of the amino acid sequences of HUC5-9 and HUC52 heavy chain CDRs and their binding abilities to LOX-1 orthologs are listed in Table. III-3. The sequence of CDR-H2 of HUC5-9 was different from that of HUC52 in 6 amino acid residues. $S52^{H}$, $G55^{H}$, and $S56^{H}$ in CDR-H2, which bound to the epitopes on human CTLD in the above simulated complex model, were maintained in both HUC52 and HUC5-9 mAb. $Y57^{H}$ of HUC52 was also important for an extensive interaction with the CTLD surface (Fig. III-6), however, it was changed to threonine residue in HUC5-9. The region of the first half of CDR-H3 of HUC52 ($C99^{H}$-$C107^{H}$) was completely identical to the corresponding region of HUC5-9 (Table. III-3). On the other hand, the second half of CDR-H3 of HUC5-9 was completely different from that of HUC52. The amino acid residues maintained in the CDRs of both HUC52 and HUC5-9 would mean that they can bind to epitopes conserved in humans, pigs and rabbit LOX-1 CTLD orthologs, or are likely to be necessary to keep the antigen binding. This fact is

consistent with above HUC52 Fab-CTLD dimer complex model, suggesting that $S52^{H}$ in CDR-H2 and the region of $C99^{H}$-$C107^{H}$ in CDR-H3 of HUC52 be important for CTLD recognition (Fig. III-5 A). And this should be an evidence supporting the validity of this model. On the other hand, the amino acid residues changed between HUC52 and HUC5-9 would either recognize the epitope amino acid residues on CTLD that are conserved in human and pig LOX-1 CTLD but not in rabbit and mouse LOX-1 orthologs, or not be involved in CTLD binding.

The amino acid residues conserved in human and pig but not in rabbit and mouse CTLD orthologs were confirmed from the sequence alignment (Fig. III-8), then three amino residues, D189, R248 and Q272 of CTLD emerged. Since D189 and Q272 are far away from the OxLDL interface on CTLD dimer, it is unlikely that these amino acid residues are recognized by the antibody. On the other hand, R248 in human and pig CTLD changes to lysine (Lys) in rabbit CTLD. Although both Arg and Lys side chains have a positive charge, HUC5-9 might have recognized sensitively subtle shape changes in the side chain structure and did not bind to rabbit CTLD. In the complex model presented in this study, R248 of human CTLD was a key epitope that interacts closely with $Y101^{H}$ on CDR-H3 of HUC52. In addition to that, a new estimation that R248 of CTLD is also recognized by $Y57^{H}$ of HUC52 or $T57^{H}$ of HUC 5-9 simultaneously with $Y101^{H}$ could be added by this consideration. This does not contradict the above complex model. This is because, as shown in Fig. III-6 B, $Y57^{H}$ of HUC52 and R248 of CTLD are in a positional relationship that they can interact sufficiently if the directions of their side chains changed. The threonine side chain of HUC5-9 whose length is shorter than that of tyrosine might not be able to form a sufficient interaction with the Lys only on rabbit CTLD.

We also discuss furthermore on the possibility that the second half region of CDR-H3 ($D108^{H}$-$S111^{H}$) of HUC52 may interact with the periphery of R248 of CTLD, which emerged from the comparison of HUC52 and HUC5-9. In the HUC52 Fab with disulfide 3D model, the CDR-H3 formed a β-hairpin structure, and the region of $D108^{H}$-$S111^{H}$ worked as the basis of β-sheet (Fig. III-1 A), so it was conceivable that this region would not be involved in antigen binding. However, the χ3 dihedral angle of the disulfide between $C99^{H}$ and $C107^{H}$ in CDR-H3 of HUC52 was 153° in the above Fab model (Fig. III-1 A), therefore it should be taken into consideration that the disulfide is exposed to more physical stress than one with a normal disulfide χ3 angle (about 90°). In that respect, there is a small possibility that the region of $D108^{H}$-$S111^{H}$ in CDR-H3 formed a second short loop rather than the basis of a β-sheet. In case of HUC5-9, the corresponding second half region in CDR-H3 has been inserted two amino acid residues for a total of six residues (Table. III-3). Therefore, this region of HUC5-9 may have a more flexible structure than HUC52. However, the amino acid sequences of that region of HUC52 (DGSS) and that of HUC5-9 (GLSADI) was completely different in both. Therefore it is unlikely that both sequences function in the same way to recognize R248 on CTLD. Rather, it would be natural to think that those regions are not involved in antigen binding.

Taken together, above HUC52 Fab-CTLD dimer complex model could reasonably explain not only HUC52

but also another anti-LOX-1 mAb HUC5-9 for the discrimination mechanism against LOX-1 orthologs. From these considerations, it is conceivable that the HUC52 Fab-CTLD recognition mechanism proposed in this study could reflect the real one in a considerable part. Of course, to fully elucidate the shape of the CDR-H3 and the antigen recognition mechanism of HUC52 Fab, experimental analysis approaches would be needed. This is a future task.

III-5. Conclusions

This study has estimated 3D structural models of HUC52 Fab and complex with human LOX-1 CTLD dimer, and their interaction mechanism. CDR-H3 of HUC52 shaped a β hairpin like structure by being bridged with a disulfide bond between $C99^{H}$ and $C107^{H}$. HUC52 bound to CTLD dimer so as to mask OxLDL binding interface. The region of $Y101^{H}$-$Y105^{H}$ (CDR-H3), $S52^{H}$-$Y57^{H}$ (CDR-H2), and $D31^{H}$ (CDR-H1) of HUC52 Fab heavy chain interacted with their epitopes. In particular, $S52^{H}$, $Y101^{H}$, $S103^{H}$ and $Y105^{H}$ formed hydrogen bonds with CTLD. Twenty-five residues on CTLD dimer were estimated as epitopes. Of these, six residues (S160, Q192, S198, S199, F200 and R248) of LOX-1 emerged as key epitopes for the cross-reactivity of HUC52 to LOX-1 orthologs. This simulated HUC52 Fab-CTLD dimer complex model could explain logically the cross-reactivity of HUC52 to LOX-1 orthologs. In case of lacking of the disulfide, CDR-H3 shaped a random coil structure, and the binding of $Y105^{H}$ on CDR-H3 to CTLD were lost completely. These results suggested that HUC52 need the disulfide in CDR-H3 and involvement of $Y105^{H}$ for the specific and high affinity CTLD binding.

III-6. Figures and Tables

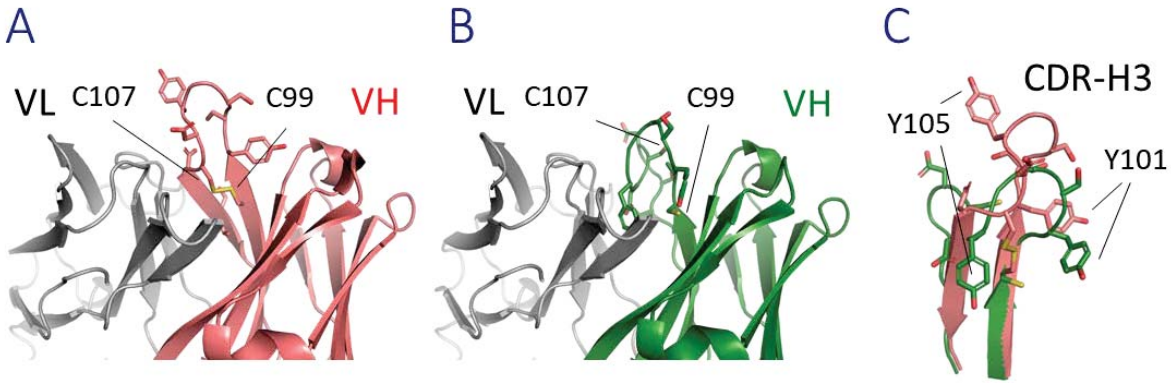

Fig. III-1.

Three-dimensional structure models of HUC52 Fab with or without disulfide bond in CDR-H3. (**A**) Fab with disulfide. The χ3 dihedral angle of the disulfide was 153.125 degree. (**B**) Fab without disulfide. In both panel, side chains of CDR-H3 are shown by stick model. Red parts are oxygen atoms, and yellow parts are sulfur atoms. (**C**) Overlay of CDR-H3 with and without disulfide.

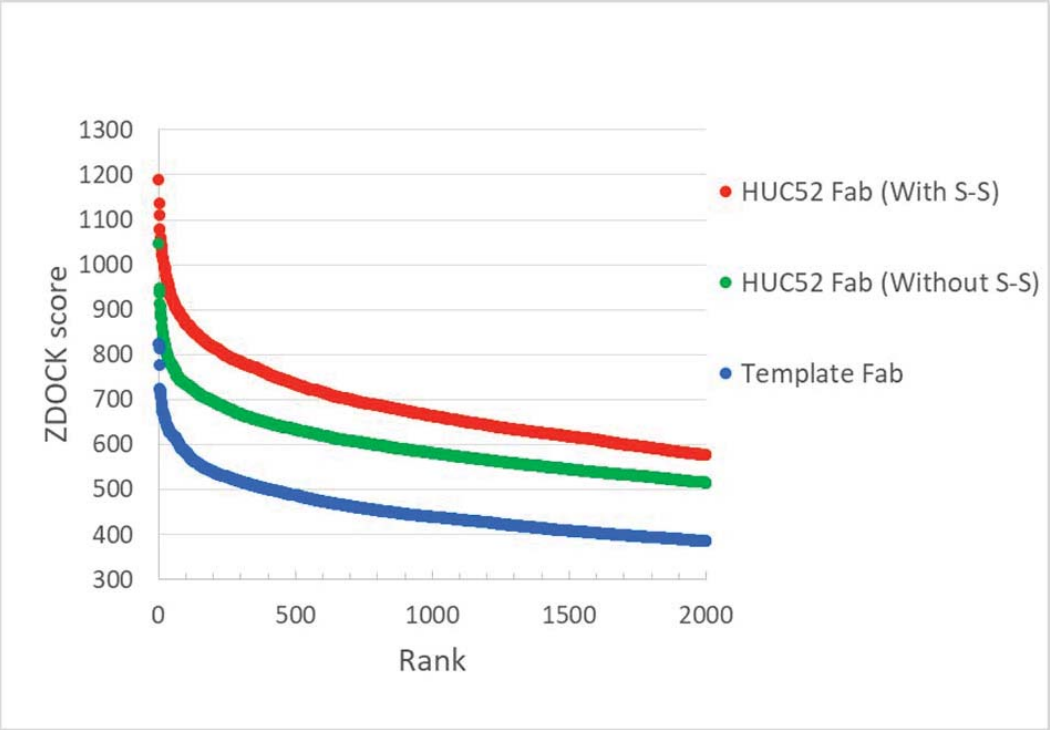

Fig. III-2.

Distribution of ZDOCK scores for the complex models of CTLD dimer and each Fab ligand. ZDOCK scores of each complex model were plotted. The X axis is the ranks, and the Y axis is the ZDOCK scores. Red represents HUC52 Fab with disulfide in CDR-H3. Green represents HUC52 Fab without disulfide. Blue represents template Fab.

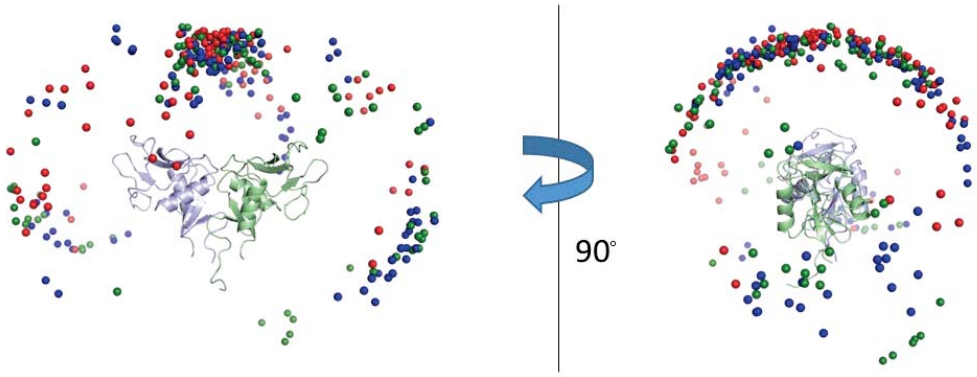

Fig. III-3.

Spatial distributions of center of mass of Fabs binding to CTLD dimer. Positions of center of mass of Fab ligands within the top 100 ZDOCK scores were plotted. CTLD dimer is shown as cartoon model. Red dots represents HUC52 Fab with disulfide. Green dots are HUC52 Fab without disulfide. Blue dots represents template Fab.

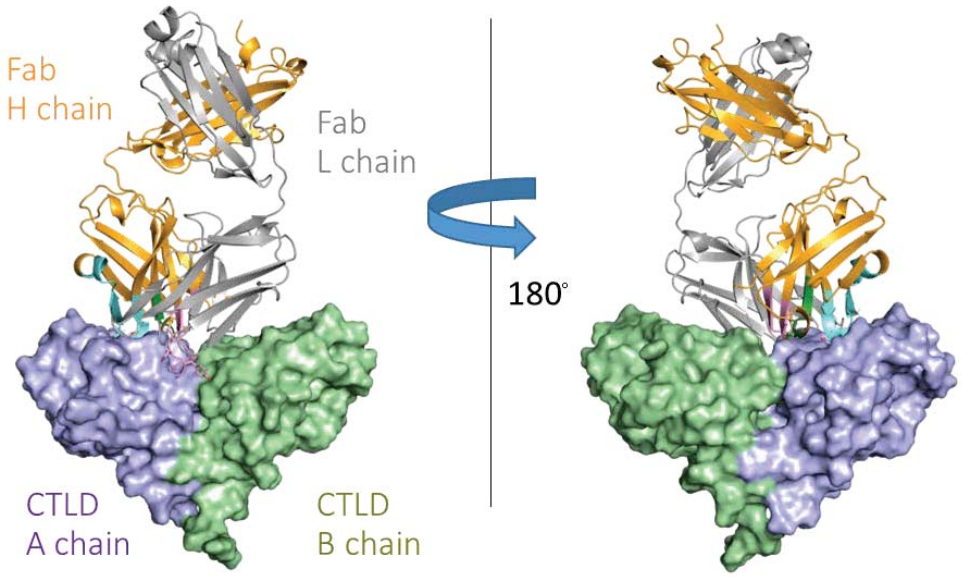

Fig. III-4.

Overall picture of HUC52 Fab with disulfide-CTLD dimer complex model. In Fab heavy chain, CDR-H1 is shown in dark green, CDR-H2 is shown in light blue, CDR-H3 is shown in pink, and FR and CH1 domain are shown in orange.

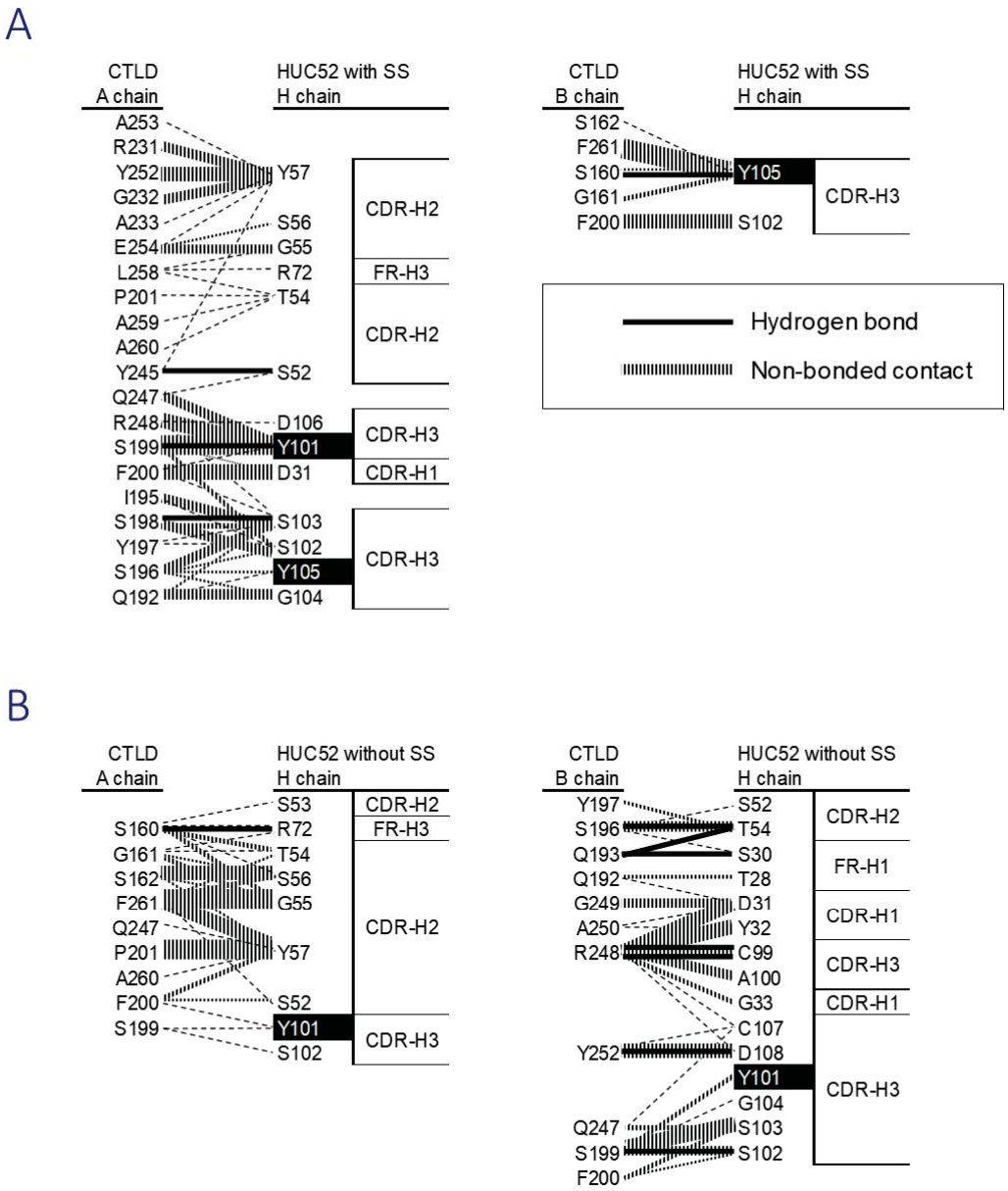

Fig. III-5.

Correlation diagrams between epitopes and paratopes. (**A**) HUC52 Fab with disulfide in CDR-H3. (**B**) HUC52 Fab without the disulfide. Solid line represents hydrogen bond. Dashed line represents non-bonding atomic contact. The thickness of dashed line reflects that more atoms are in contact.

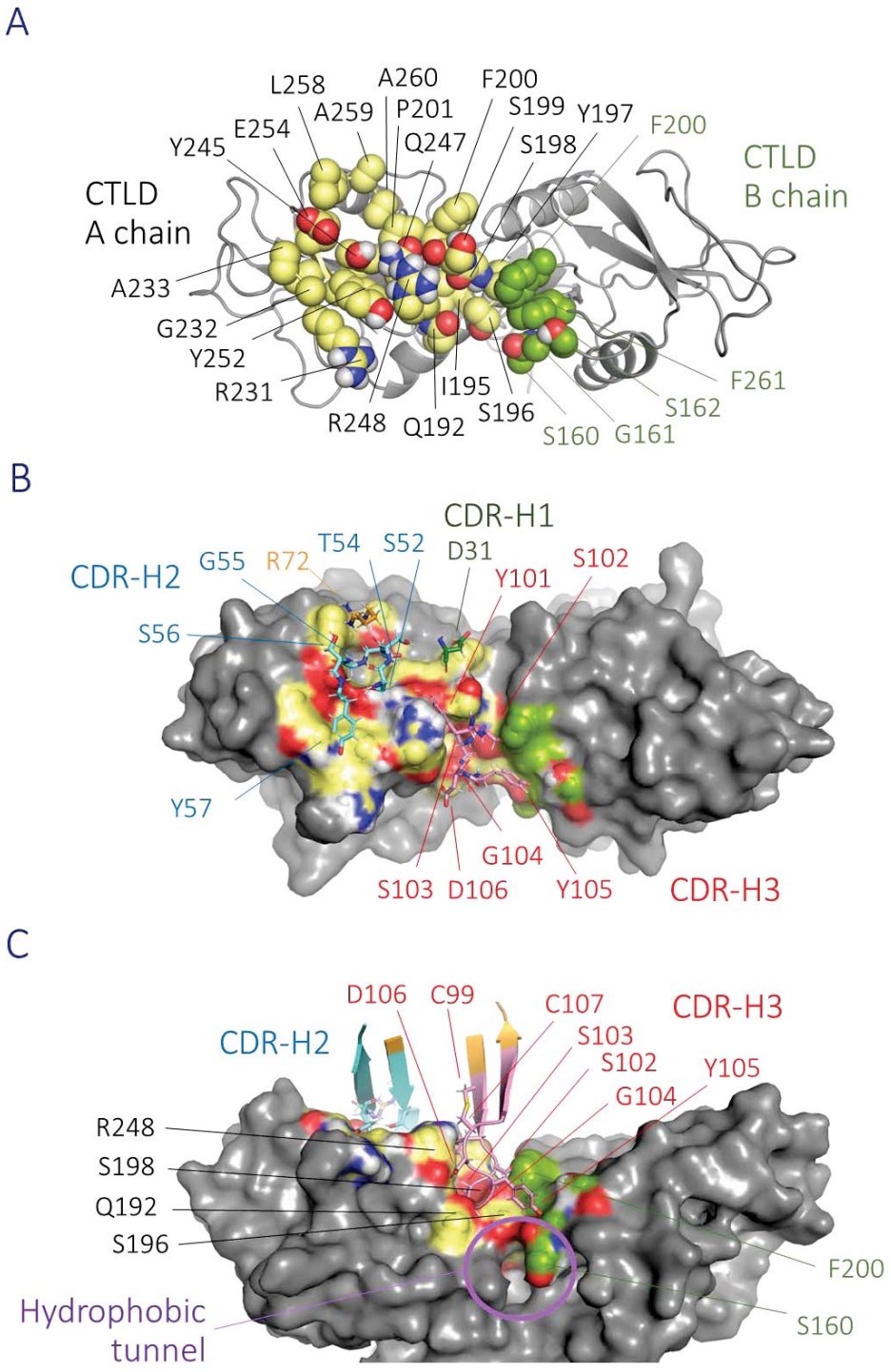

Fig. III-6.

Epitopes and paratopes on complex model of CTLD dimer and HUC52 Fab with disulfide in CDR-H3. (**A**) Epitopes on CTLD dimer. (**B**) VH paratopes binding to CTLD dimer. (**C**) Enlarged front view around CDR-H3.

In all panels, CDR-H1 is shown in dark green, CDR-H2 is shown in light blue, CDR-H3 is shown in pink, and framework regions are shown in orange. Only atoms of epitope residues on CTLD dimer were colored. Light yellow: carbon atoms of epitope residues on CTLD A-chain, Pale green: those on B-chain. Hydrogen atoms (white spheres) were displayed only to polar groups of side chains of epitope residues for ease of viewing. Red parts are oxygen atoms, blue parts are nitrogen atoms.

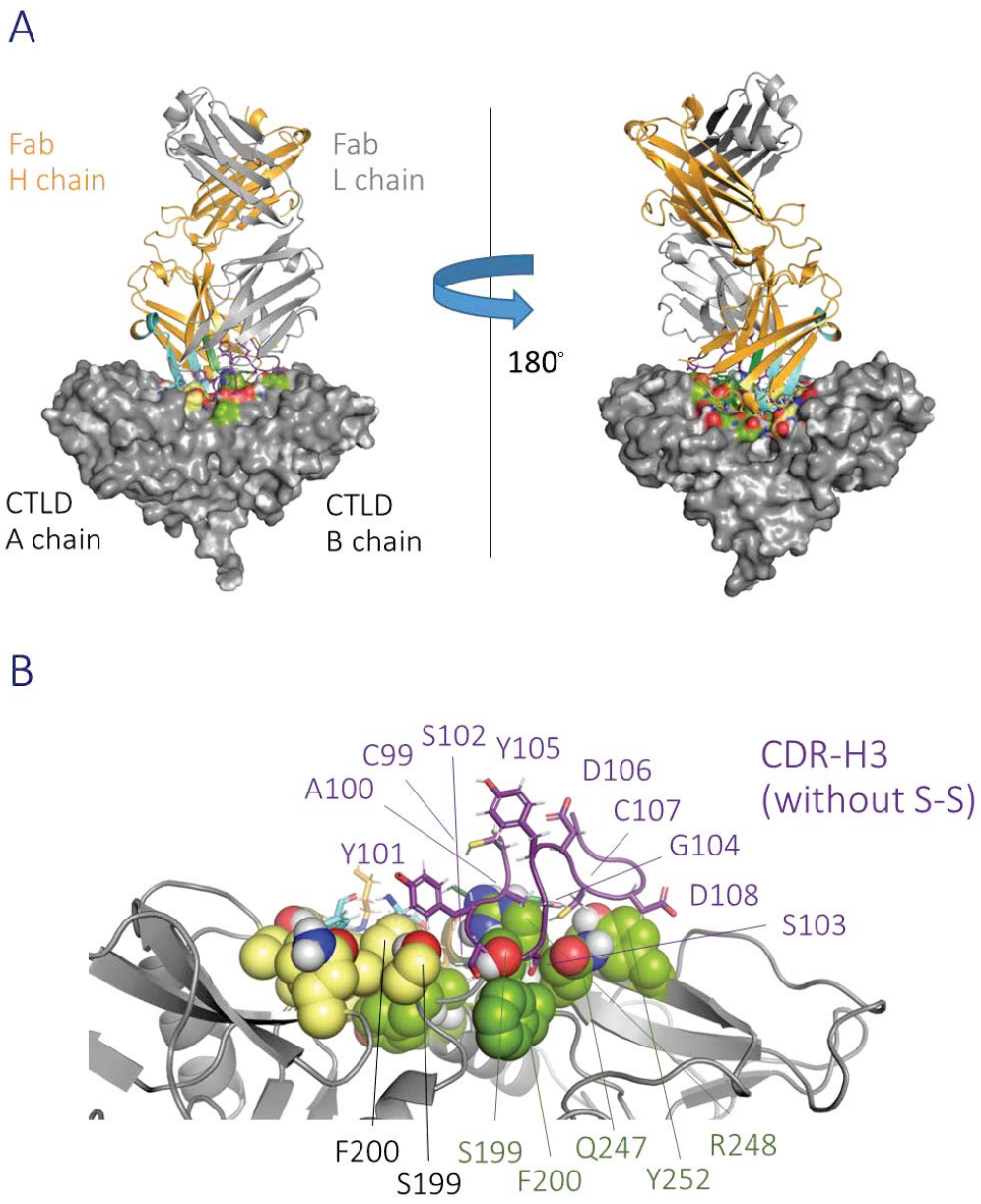

Fig. III-7.

Complex model of CTLD dimer and HUC52 Fab without disulfide in CDR-H3. (**A**) Overall picture. (**B**) Enlarged view around CDR-H3. In both panels, CDR-H3 is shown in purple. In other respects, the meanings of each color are the same as in Fig. III-6.

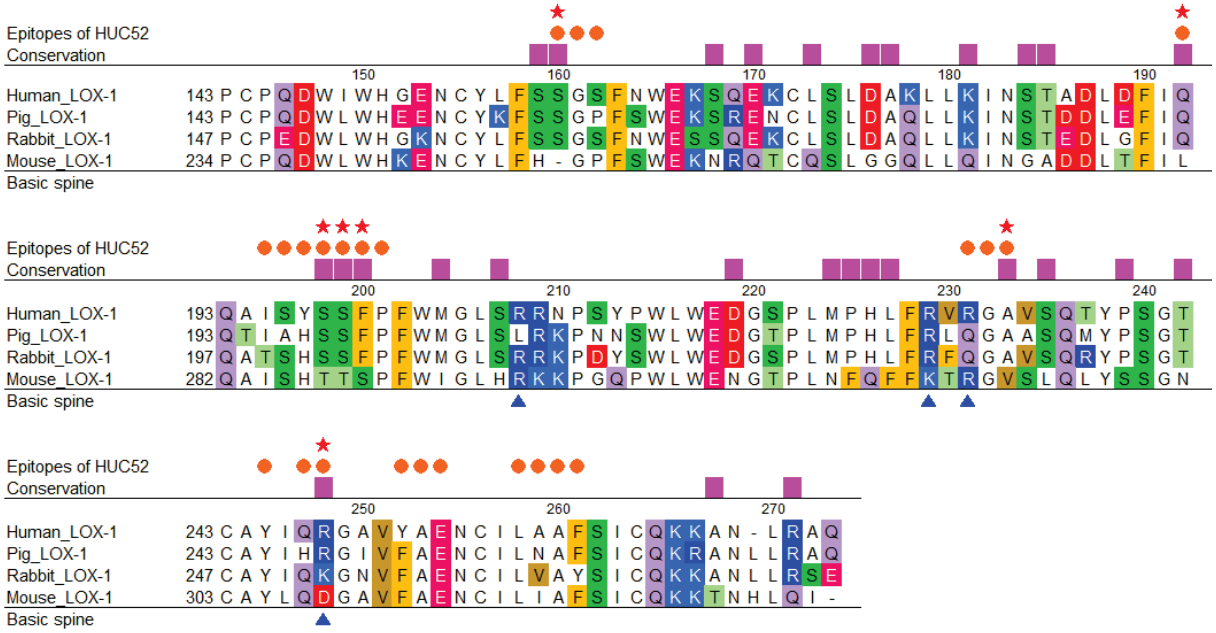

Fig. III-8.

Sequence alignment of LOX-1 CTLD orthologs. Comparison of human, pig, rabbit and mouse LOX-1 CTLD are shown. Residues identified as epitopes are marked with orange circles. Residues that are conserved among human, pig, rabbit LOX-1 but not conserved in mouse LOX-1 are marked with pink squares. Here we regarded as changes between R and K are conserved. Red star marks represent the residues in which both of orange circle and pink square are overlapping. Basic spine residues are marked with blue triangle.

Table. III-1.

Amino acid sequences of heavy chain CDRs of HUC52[a]

Region	Sequence
CDR-H1	DYGMG
CDR-H2	VISSTGSYTNYGSAVK
CDR-H3	CAYSSGYDCDGSS

[a] Cited from published patent information [90].

Table. III-2.

List of interactions between HUC52 Fab and CTLD dimer of the 1st ranked complex models

Ligand	ZDOCK score	No. of Hydrogen bonds[a]	No. of non-bonded contacts[a]
HUC52 Fab with disulfide in CDR-H3	1189.735	4 (A-H: 3) (B-H: 1)	308 (A-H:267) (B-H: 32) (A-L: 1) (B-L: 8)
HUC52 Fab without disulfide in CDR-H3	1047.274	8 (A-H: 1) (B-H: 7)	368 (A-H:145) (B-H:223)

[a] Alphabets in parentheses mean molecular chains, and numbers mean the number of bonds or contacts formed. A: CTLD A-chain, B: CTLD B-chain, H: Fab heavy chain, L: Fab light chain.

Table. III-3

Comparison list of HUC52 and HUC5-9 anti-LOX-1 mAb

	Amino acid sequences of heavy chain CDRs [a]			Binding to LOX-1 orthologs [b]			
Regions	CDR-H1	CDR-H2	CDR-H3				
Residue No.	3 1 2 3 4 5	5 0 1 2 3 4 5 6 7 8 9 0 1 2 3 4 5	1 9 0 1 2 3 4 5 6 7 7 7 8 9 0 1 a b	Human	Pig	Rabbit	Mouse
HUC52 [c]	D Y G M G	**V** I S **S** **T** G S **Y** T **N** Y G **S** A V K	C A Y S S G Y D C - - **D** **G** **S** **S**	Yes	Yes	**Yes**	No
HUC5-9 [c]	D Y G M G	**E** I S **A** **A** G S **T** T **F** Y G **A** A V K	C A Y S S G Y D C **G** **L** **S** **A** **D** **I**	Yes	Yes	**No**	No

[a] Cited from published patent information [90].

[b] Cited from the previous study by Iwamoto *et al* [42].

[c] Differences between HUC52 and HUC5-9 are shown in bold to highlight.

Table. III-S1

Amino acid sequences of template chicken-human IgG1λ chimeric antibody Fab

Chain	Region	Sequence [a]
Heavy chain	FR-H1	AVTLDESGGGLQTPGGGLSLVCKASGFTLS
	CDR-H1	SYQMM
	FR-H2	WVRQAPGKGLEWVA
	CDR-H2	GITSRGGVTGYGSAVK
	FR-H3	GRATISRDNGQSTVRLQLNNLRAEDTGTYYCAK
	CDR-H3	PALDSDQCGFPEAGC
	FR-H4	IDAWGHGTEVIVSS
	CH1	ASTKGPSVFPLAPSSKSTSGGTAALGCLVKDYFPEPVTVSWNSG
		ALTSGVHTFPAVLQSSGLYSLSSVVTVPSSSLGTQTYICNVNHKPS
		NTKVDKKVEPKS
Light chain	FR-L1	ALTQPTSVSANLGGSVEITC
	CDR-L1	SGSDYDYG
	FR-L2	WYQQKAPGSAPVTVIY
	CDR-L2	WNDKRPS
	FR-L3	DIPSRFSGSTSGSTSTLTITGVQAEDEAVYYC
	CDR-L3	GAYDGSAGGGI
	FR-L4	FGAGTTLTVLG
	CL	QPKAAPSVTLFPPSSEELQANKATLVCLISDFYPGAVTVAWKADS
		SPVKAGVETTTPSKQSNNKYAASSYLSLTPEQWKSHRSYSCQVT
		HEGSTVEKTVAPTE

[a] Sequences are cited from Protein Data Bank code: 4GLR [93].

Chapter IV　General Conclusions

In this doctoral dissertation, the details of the interaction mechanisms for two different types of artificial ligands; anionic small unilamellar vesicle (SUV) and chicken-derived monoclonal antibody (mAb) which specifically bind to LOX-1 were studied and discussed. This is because these are promising agents for LOX-1 targeting therapy.

In chapter II, SUVs composed of negatively charged phospholipid DOPG or neutrally charged phospholipid DOPC were prepared in different sizes (70 nm or 124 nm in diameter), and their affinities toward LOX-1 clusters immobilized on the self-assembled monolayer (SAM)-SPR sensors were compared to AcLDL (a chemically stable surrogate reference substance equivalent to OxLDL). As a result, anionic DOPG-SUV sized with 30 nm pore diameter filter (DOPG-SUV30) demonstrated about 20 times stronger affinity to LOX-1 ECD clusters than AcLDL. DOPG-SUV30 had the negative surface charge comparable to AcLDL (-42 mV), and its size (70 nm) was about twice that of AcLDL. This indicated the enhancement of LOX-1 affinity correlated with the size of negatively charged ligand, and it was due to the multivalent interaction of more LOX-1s with DOPG-SUV 30 particle than with AcLDL. Furthermore, a competitive cellular uptake assay using LOX-1 expressing cells demonstrated that DOPG-SUV30 was internalized more preferentially into living cells than AcLDL, even in the presence of a 150 fold excess amount of AcLDL. DOPG-SUV100 (-42 mV, 124 nm) showed almost the same LOX-1 affinity as that of DOPG-SUV30. These results indicated that the affinity with LOX-1 clusters was not further enhanced even if the particle size exceeds 70 nm. This was probably due to the fact that the more bulky DOPG-SUV100 had a larger size exclusion effect to unbound particles on LOX-1 clusters plane. This means that there is an optimum particle size (70 nm) in ligand binding onto LOX-1 clusters surface. In case of DOPC-SUV30 (-8.4 mV, 68 nm), the affinity was lost due to the neutral surface charge. As for the safety, DOPG-SUV30 did not show a cell teratogenicity and VCAM-1 induction, which is a biomarker of cellular dysfunction triggered by LOX-1 signaling, indicating a low risk of safety for *in vivo* use. Taken together, this study demonstrated that DOPG-SUV30 can function as a DDS carrier targeting to LOX-1 expressing pathological sites of atherosclerosis and cancer at least for *in vitro* use.

In chapter III, Fab domain of chicken-derived anti-LOX-1 mAb HUC52 and the complex model with LOX-1 CTLD homodimer were constructed by computer simulation approach to estimate their epitopes and paratopes interaction. CDR-H3 of HUC52 shaped a β hairpin like structure by being bridged with a disulfide bond between $C99^{H}$ and $C107^{H}$. HUC52 Fab bound to CTLD dimer so as to mask the OxLDL binding

interface. The regions of $Y101^{H}$ - $Y105^{H}$ (CDR-H3), $S52^{H}$ - $Y57^{H}$ (CDR-H2), $D31^{H}$ (CDR-H1) of HUC52 Fab heavy chain interacted with their epitopes. In particular, $S52^{H}$, $Y101^{H}$, $S103^{H}$ and $Y105^{H}$ formed hydrogen bonds with CTLD. Twenty-five residues on CTLD dimer were estimated as epitopes. Of these, six residues (S160, Q192, S198, S199, F200 and R248) of LOX-1 emerged as key epitopes for the cross-reactivity of HUC52 to LOX-1 orthologs. This simulated HUC52 Fab-CTLD dimer complex model could explain logically the cross-reactivity of HUC52 to LOX-1 orthologs. In case of lacking of the disulfide, CDR-H3 shaped a random coil structure, and the binding of $Y105^{H}$ on CDR-H3 to CTLD were lost completely. This study suggested that HUC52 need the disulfide in CDR-H3 and involvement of $Y105^{H}$ for the specific and high affinity CTLD binding.

The two studies carried out in this doctoral dissertation have revealed that nano-liposome (DOPG-SUV30) and monoclonal antibody (HUC52) each specifically bind to LOX-1 CTLD and inhibit OxLDL uptake by entirely different mechanisms. I believe these findings contribute to the development of LOX-1 selective DDS carriers and biopharmaceuticals that will be used for LOX-1 targeting therapy in the future. But there are still many issues to be solved in order to bring and use them in actual clinical sites, such as their manufacturing costs, risks of toxicity and stability, and conflicting patents. Both nano-liposomes and mAbs have advantages and disadvantages in these respects, they are each expected to make further progress in their research and overcome the bottlenecks, respectively. I am convinced that the practical application and commercialization of LOX-1 targeting therapy is one of the remaining challenges in the medical and pharmaceutical industry to be achieved. This should bring healthy lives to people all over the world.

Acknowledgments

This doctoral dissertation is a summary of the research results I have been enrolled in the doctoral program of the Department of Mathematical and Life sciences, Graduate School of Science, Hiroshima University.

I would like to express my deep gratitude to Professor Shin-ichi Tate for giving me the opportunity to conduct my doctoral research, and for his patient guidance throughout the years.

I would like to express my grateful to Dr. Naoya Tochio, Senior Lecturer of Faculty of Pharma-Sciences, Teikyo University, for his guidance and numerous valuable advice, especially for the research in chapter III.

I would like to thank Professor Shuichi Furusawa and Professor Hiroyuki Horiuchi, Graduate School of Biosphere Science, Hiroshima University for their helpful advices.

Finally, I deeply grateful to my family for their affectionate supports over many years.

References

[1] WHO, The top 10 causes of death, 2017.

[2] R. Ross, The pathogenesis of atherosclerosis: a perspective for the 1990s., Nature. 362 (1993) 801–9. doi:10.1038/362801a0.

[3] K.J. Williams, I. Tabas, The Response-to-Retention Hypothesis of Early Atherogenesis, Arterioscler. Thromb. Vasc. Biol. 15 (1995) 551–561. doi:10.1161/01.ATV.15.5.551.

[4] D. Steinberg, S. Parthasarathy, T.E. Carew, J.C. Khoo, J.L. Witztum, Beyond cholesterol. Modifications of low-density lipoprotein that increase its atherogenicity., N. Engl. J. Med. 320 (1989) 915–924. doi:10.1056/NEJM198904063201407.

[5] R. Yoshimoto, Y. Fujita, A. Kakino, S. Iwamoto, T. Takaya, T. Sawamura, The discovery of LOX-1, its ligands and clinical significance, Cardiovasc. Drugs Ther. 25 (2011) 379–391. doi:10.1007/s10557-011-6324-6.

[6] A. Pirillo, G.D. Norata, A.L. Catapano, LOX-1, OxLDL, and atherosclerosis, Mediators Inflamm. 2013 (2013). doi:10.1155/2013/152786.

[7] A.J. Kattoor, S.H. Kanuri, J.L. Mehta, Role of Ox-LDL and LOX-1 in Atherogenesis., Curr. Med. Chem. 25 (2018) 1–8. doi:10.2174/0929867325666180508100950.

[8] T. Sawamura, N. Kume, T. Aoyama, H. Moriwaki, H. Hoshikawa, Y. Aiba, T. Tanaka, S. Miwa, Y. Katsura, T. Kita, T. Masaki, An endothelial receptor for oxidized low-density lipoprotein., Nature. 386 (1997) 73–77. doi:10.1038/386073a0.

[9] T. Aoyama, T. Sawamura, Y. Furutani, R. Matsuoka, M.C. Yoshida, H. Fujiwara, T. Masaki, Structure and chromosomal assignment of the human lectin-like oxidized low-density-lipoprotein receptor-1 (LOX-1) gene., Biochem. J. 339 (1999) 177–84. doi:10.1042/0264-6021:3390177.

[10] X. Shi, S. Niimi, T. Ohtani, S. Machida, Characterization of residues and sequences of the carbohydrate recognition domain required for cell surface localization and ligand binding of human lectin-like oxidized LDL receptor., J. Cell Sci. 114 (2001) 1273–1282. http://www.ncbi.nlm.nih.gov/pubmed/11256994.

[11] M. Chen, S. Narumiya, T. Masaki, T. Sawamura, Conserved C-terminal residues within the lectin-like domain of LOX-1 are essential for oxidized low-density-lipoprotein binding., Biochem. J. 355 (2001) 289–296. doi:10.1042/0264-6021:3550289.

[12] H. Kataoka, N. Kume, S. Miyamoto, M. Minami, H. Moriwaki, T. Murase, T. Sawamura, T. Masaki, N. Hashimoto, T. Kita, Expression of Lectinlike Oxidized Low-Density Lipoprotein Receptor-1 in Human Atherosclerotic Lesions, Circulation. 99 (1999) 3110–3117. doi:10.1161/01.CIR.99.24.3110.

[13] L. Maldonado-Báez, C. Williamson, J.G. Donaldson, Clathrin-independent endocytosis: A cargo-centric view, Exp. Cell Res. 319 (2013) 2759–2769. doi:10.1016/j.yexcr.2013.08.008.

[14] J.E. Murphy, R.S. Vohra, S. Dunn, Z.G. Holloway, A.P. Monaco, S. Homer-Vanniasinkam, J.H. Walker, S.

Ponnambalam, Oxidised LDL internalisation by the LOX-1 scavenger receptor is dependent on a novel cytoplasmic motif and is regulated by dynamin-2, J. Cell Sci. 121 (2008) 2136–2147. doi:10.1242/jcs.020917.

[15] M. Kumano-Kuramochi, Q. Xie, S. Kajiwara, S. Komba, T. Minowa, S. Machida, Lectin-like oxidized LDL receptor-1 is palmitoylated and internalizes ligands via caveolae/raft-dependent endocytosis, Biochem. Biophys. Res. Commun. 434 (2013) 594–599. doi:10.1016/j.bbrc.2013.03.120.

[16] I. Ohki, T. Ishigaki, T. Oyama, S. Matsunaga, Q. Xie, M. Ohnishi-Kameyama, T. Murata, D. Tsuchiya, S. Machida, K. Morikawa, S. Tate, Crystal structure of human lectin-like, oxidized low-density lipoprotein receptor 1 ligand binding domain and its ligand recognition mode to OxLDL, Structure. 13 (2005) 905–917. doi:10.1016/j.str.2005.03.016.

[17] S. Tate, Structure and mode of ligand recognition of the oxidized LDL receptor, LOX-1, Funct. Struct. Biol. Lipo-Network, Transw. Res. Netw. 661 (2006) 179–198.

[18] T. Ishigaki, I. Ohki, N. Utsunomiya-Tate, S. Tate, Chimeric structural stabilities in the coiled-coil structure of the NECK domain in human lectin-like oxidized low-density lipoprotein receptor 1 (LOX-1), J. Biochem. 141 (2007) 855–866. doi:10.1093/jb/mvm093.

[19] I. Ohki, H. Amida, R. Yamada, M. Sugihara, T. Ishigaki, S. Tate, Surface plasmon resonance study on functional significance of clustered organization of lectin-like oxidized LDL receptor (LOX-1), Biochim. Biophys. Acta. 1814 (2011) 345–354. doi:10.1016/j.bbapap.2010.10.006.

[20] S. Nakano, M. Sugihara, R. Yamada, K. Katayanagi, S.I. Tate, Structural implication for the impaired binding of W150A mutant LOX-1 to oxidized low density lipoprotein, OxLDL, Biochim. Biophys. Acta. 1824 (2012) 739–749. doi:10.1016/j.bbapap.2012.02.003.

[21] S. Xu, S. Ogura, J. Chen, P.J. Little, J. Moss, P. Liu, LOX-1 in atherosclerosis: Biological functions and pharmacological modifiers, Cell. Mol. Life Sci. 70 (2013) 2859–2872. doi:10.1007/s00018-012-1194-z.

[22] H.H. Shih, S. Zhang, W. Cao, A. Hahn, J. Wang, J.E. Paulsen, D.C. Harnish, CRP is a novel ligand for the oxidized LDL receptor LOX-1, Am. J. Physiol. Circ. Physiol. 296 (2009) H1643–H1650. doi:10.1152/ajpheart.00938.2008.

[23] M. Murdocca, R. Mango, S. Pucci, S. Biocca, B. Testa, R. Capuano, R. Paolesse, M. Sanchez, A. Orlandi, C. di Natale, G. Novelli, F. Sangiuolo, The lectin-like oxidized LDL receptor-1: a new potential molecular target in colorectal cancer., Oncotarget. 7 (2016) 14765–80. doi:10.18632/oncotarget.7430.

[24] I. González-Chavarría, R.P. Cerro, N.P. Parra, F.A. Sandoval, F.A. Zuñiga, V.A. Omazábal, L.I. Lamperti, S.P. Jiménez, E.A. Fernandez, N.A. Gutiérrez, F.S. Rodriguez, S.A. Onate, O. Sánchez, J.C. Vera, J.R. Toledo, Lectin-like oxidized LDL receptor-1 is an enhancer of tumor angiogenesis in human prostate cancer cells., PLoS One. 9 (2014) e106219. doi:10.1371/journal.pone.0106219.

[25] M. Khaidakov, S. Mitra, B.Y. Kang, X. Wang, S. Kadlubar, G. Novelli, V. Raj, M. Winters, W.C. Carter, J.L. Mehta, Oxidized LDL receptor 1 (OLR1) as a possible link between obesity, dyslipidemia and cancer, PLoS One. 6 (2011) 1–9. doi:10.1371/journal.pone.0020277.

[26] S. Balzan, V. Lubrano, LOX-1 receptor: A potential link in atherosclerosis and cancer., Life Sci. 198 (2018) 79–86. doi:10.1016/j.lfs.2018.02.024.

[27] J. Lu, S. Mitra, X. Wang, M. Khaidakov, J.L. Mehta, Oxidative Stress and Lectin-Like Ox-LDL-Receptor LOX-1 in Atherogenesis and Tumorigenesis, Antioxid. Redox Signal. 15 (2011) 2301–2333. doi:10.1089/ars.2010.3792.

[28] J. Jiang, M. Yan, J.L. Mehta, C. Hu, Angiogenesis is a link between atherosclerosis and tumorigenesis: Role of LOX-1, Cardiovasc. Drugs Ther. 25 (2011) 461–468. doi:10.1007/s10557-011-6343-3.

[29] J.C. Sluimer, M.J. Daemen, Novel concepts in atherogenesis: angiogenesis and hypoxia in atherosclerosis, J. Pathol. 218 (2009) 7–29. doi:10.1002/path.2518.

[30] A. Dandapat, C. Hu, L. Sun, J.L. Mehta, Small concentrations of OXLDL induce capillary tube formation from endothelial cells via LOX-1-dependent redox-sensitive pathway, Arterioscler. Thromb. Vasc. Biol. 27 (2007) 2435–2442. doi:10.1161/ATVBAHA.107.152272.

[31] F. Wan, X. Qin, G. Zhang, X. Lu, Y. Zhu, H. Zhang, B. Dai, G. Shi, D. Ye, Oxidized low-density lipoprotein is associated with advanced-stage prostate cancer, Tumor Biol. 36 (2015) 3573–3582. doi:10.1007/s13277-014-2994-6.

[32] M. Liang, P. Zhang, J. Fu, Up-regulation of LOX-1 expression by TNF-α promotes trans-endothelial migration of MDA-MB-231 breast cancer cells, Cancer Lett. 258 (2007) 31–37. doi:10.1016/j.canlet.2007.08.003.

[33] C. Li, J. Zhang, H. Wu, L. Li, C. Yang, S. Song, P. Peng, M. Shao, M. Zhang, J. Zhao, R. Zhao, W. Wu, Y. Ruan, L. Wang, J. Gu, Lectin-like oxidized low-density lipoprotein receptor-1 facilitates metastasis of gastric cancer through driving epithelial-mesenchymal transition and PI3K/Akt/GSK3β activation, Sci. Rep. 7 (2017) 1–12. doi:10.1038/srep45275.

[34] J. Zhang, L. Zhang, C. Li, C. Yang, L. Li, S. Song, H. Wu, F. Liu, L. Wang, J. Gu, LOX-1 is a poor prognostic indicator and induces epithelial-mesenchymal transition and metastasis in pancreatic cancer patients, Cell. Oncol. 41 (2018) 73–84. doi:10.1007/s13402-017-0360-6.

[35] L. Jiang, S. Jiang, Y. Lin, H. Yang, Z. Zhao, Z. Xie, Y. Lin, H. Long, Combination of body mass index and oxidized low density lipoprotein receptor 1 in prognosis prediction of patients with squamous non-small cell lung cancer, Oncotarget. 6 (2015). doi:10.18632/oncotarget.4299.

[36] M. Akagi, A. Ueda, T. Teramura, S. Kanata, T. Sawamura, C. Hamanishi, Oxidized LDL binding to LOX-1 enhances MCP-1 expression in cultured human articular chondrocytes, Osteoarthr. Cartil. 17 (2009) 271–275. doi:10.1016/j.joca.2008.06.019.

[37] M. Ishikawa, H. Ito, M. Akiyoshi, N. Kume, H. Yoshitomi, H. Mitsuoka, S. Tanida, K. Murata, H. Shibuya, T. Kasahara, A. Kakino, Y. Fujita, T. Sawamura, T. Yasuda, T. Nakamura, Lectin-like oxidized low-density lipoprotein receptor 1 signal is a potent biomarker and therapeutic target for human rheumatoid arthritis., Arthritis Rheum. 64 (2012) 1024–1034. doi:10.1002/art.33452.

[38] Z. Ding, S. Liu, X. Wang, X. Deng, Y. Fan, J. Shahanawaz, R.J.S. Reis, K.I. Varughese, T. Sawamura, J.L. Mehta, Cross-Talk between LOX-1 and PCSK9 in vascular tissues, Cardiovasc. Res. 107 (2015) 556–567.

doi:10.1093/cvr/cvv178.

[39] M.T. Gürgöze, A.H.G. Muller-Hansma, M.M. Schreuder, A.M.H. Galema-Boers, E. Boersma, J.E. Roeters van Lennep, Adverse events associated with PCSK9 inhibitors: A real-world experience, Clin. Pharmacol. Ther. 105 (2019) 496–504. doi:10.1002/cpt.1193.

[40] M. Falconi, S. Ciccone, P. D'Arrigo, F. Viani, R. Sorge, G. Novelli, P. Patrizi, A. Desideri, S. Biocca, Design of a novel LOX-1 receptor antagonist mimicking the natural substrate, Biochem. Biophys. Res. Commun. 438 (2013) 340–345. doi:10.1016/j.bbrc.2013.07.073.

[41] S. Thakkar, X. Wang, M. Khaidakov, Y. Dai, K. Gokulan, J.L. Mehta, K.I. Varughese, Structure-based Design Targeted at LOX-1, a Receptor for Oxidized Low-Density Lipoprotein, Sci. Rep. 5 (2015) 16740. doi:10.1038/srep16740.

[42] S. Iwamoto, N. Nishimichi, Y. Tateishi, Y. Sato, H. Horiuchi, S. Furusawa, T. Sawamura, H. Matsuda, Generation and characterization of chicken monoclonal antibodies against human LOX-1, MAbs. 1 (2009) 357–363.

[43] W. Hu, Q. Xie, H. Xiang, Improved scFv Anti-LOX-1 Binding Activity by Fusion with LOX-1-Binding Peptides, Biomed Res. Int. 2017 (2017) 1–9. doi:10.1155/2017/8946935.

[44] S. Ishino, T. Mukai, Y. Kuge, N. Kume, M. Ogawa, N. Takai, J. Kamihashi, M. Shiomi, M. Minami, T. Kita, H. Saji, Targeting of Lectinlike Oxidized Low-Density Lipoprotein Receptor 1 (LOX-1) with 99mTc-Labeled Anti-LOX-1 Antibody: Potential Agent for Imaging of Vulnerable Plaque, J. Nucl. Med. 49 (2008) 1677–1685. doi:10.2967/jnumed.107.049536.

[45] A. Saito, H. Shimizu, Y. Doi, T. Ishida, M. Fujimura, T. Inoue, H. Kiwada, T. Tominaga, Immunoliposomal drug-delivery system targeting lectin-like oxidized low-density lipoprotein receptor-1 for carotid plaque lesions in rats., J. Neurosurg. 115 (2011) 720–727. doi:10.3171/2011.5.JNS10227.

[46] D. Li, A.R. Patel, A.L. Klibanov, C.M. Kramer, M. Ruiz, B.-Y. Kang, J.L. Mehta, G.A. Beller, D.K. Glover, C.H. Meyer, Molecular imaging of atherosclerotic plaques targeted to oxidized LDL receptor LOX-1 by SPECT/CT and magnetic resonance., Circ. Cardiovasc. Imaging. 3 (2010) 464–472. doi:10.1161/CIRCIMAGING.109.896654.

[47] F. Amati, L. Diano, L. Vecchione, G.D. Norata, Y. Koyama, L. Cutuli, A.L. Catapano, F. Romeo, H. Ando, G. Novelli, LOX-1 inhibition in ApoE KO mice using a schizophyllan-based antisense oligonucleotide therapy, Mol. Ther. - Nucleic Acids. 1 (2012) 1–3. doi:10.1038/mtna.2012.45.

[48] G. Vindigni, S. Raniolo, A. Ottaviani, M. Falconi, O. Franch, B.R. Knudsen, A. Desideri, S. Biocca, Receptor-Mediated Entry of Pristine Octahedral DNA Nanocages in Mammalian Cells, ACS Nano. 10 (2016) 5971–5979. doi:10.1021/acsnano.6b01402.

[49] N.V.K. Pothineni, S.K. Karathanasis, Z. Ding, A. Arulandu, K.I. Varughese, J.L. Mehta, LOX-1 in Atherosclerosis and Myocardial Ischemia: Biology, Genetics, and Modulation, J. Am. Coll. Cardiol. 69 (2017) 2759–2768. doi:10.1016/j.jacc.2017.04.010.

[50] J. De Siqueira, I. Abdul Zani, D.A. Russell, S.B. Wheatcroft, S. Ponnambalam, S. Homer-Vanniasinkam, Clinical and

Preclinical Use of LOX-1-Specific Antibodies in Diagnostics and Therapeutics, J. Cardiovasc. Transl. Res. 8 (2015) 458–465. doi:10.1007/s12265-015-9655-z.

[51] S. Matarazzo, M.C. Quitadamo, R. Mango, S. Ciccone, G. Novelli, S. Biocca, Cholesterol-Lowering Drugs Inhibit Lectin-Like Oxidized Low-Density Lipoprotein-1 Receptor Function by Membrane Raft Disruption, Mol. Pharmacol. 82 (2012) 246–254. doi:10.1124/mol.112.078915.

[52] S. Matsunaga, Q. Xie, M. Kumano, S. Niimi, K. Sekizawa, Y. Sakakibara, S. Komba, S. Machida, Lectin-like oxidized low-density lipoprotein receptor (LOX-1) functions as an oligomer and oligomerization is dependent on receptor density, Exp. Cell Res. 313 (2007) 1203–1214. doi:10.1016/j.yexcr.2007.01.007.

[53] M. Nagase, S. Hirose, T. Sawamura, T. Masaki, T. Fujita, Enhanced expression of endothelial oxidized low-density lipoprotein receptor (LOX-1) in hypertensive rats., Biochem. Biophys. Res. Commun. 237 (1997) 496–498. doi:10.1006/bbrc.1997.7176.

[54] J.L. Mehta, J. Chen, P.L. Hermonat, F. Romeo, G. Novelli, Lectin-like, oxidized low-density lipoprotein receptor-1 (LOX-1): A critical player in the development of atherosclerosis and related disorders, Cardiovasc. Res. 69 (2006) 36–45. doi:10.1016/j.cardiores.2005.09.006.

[55] M. Chen, M. Kakutani, M. Minami, H. Kataoka, N. Kume, S. Narumiya, T. Kita, T. Masaki, T. Sawamura, Increased Expression of Lectinlike Oxidized Low Density Lipoprotein Receptor-1 in Initial Atherosclerotic Lesions of Watanabe Heritable Hyperlipidemic Rabbits, Arterioscler. Thromb. Vasc. Biol. 20 (2000) 1107–1115. doi:10.1161/01.ATV.20.4.1107.

[56] H. Park, F.G. Adsit, J.C. Boyington, The 1.4 Å Crystal Structure of the Human Oxidized Low Density Lipoprotein Receptor Lox-1, J. Biol. Chem. 280 (2005) 13593–13599. doi:10.1074/jbc.M500768200.

[57] Shin-ichi Tate, Oxidized low-density lipoprotein receptor, LOX-1, on the endothelial cell-the receptor structure and functions of LOX-1 in atherogenesis, J Biol Macromol. 7 (2007) 11–22.

[58] M.A. Liebert, Q. Xie, S. Matsunaga, S. Niimi, S. Ogawa, K. Tokuyasu, Y. Sakakibara, S. Machida, Human lectin-like oxidized low-density lipoprotein receptor-1 functions as a dimer in living cells, DNA Cell Biol. 23 (2004) 111–117. doi:10.1089/104454904322759920.

[59] W. Cao, V. Calabro, A. Root, G. Yan, K. Lam, S. Olland, J. Sanford, A. Robak, R. Zollner, Z. Lu, M. Ait-Zahra, R. Agostinelli, L. Tchistiakova, D. Gill, D. Harnish, J. Paulsen, H.H. Shih, Oligomerization is required for the activity of recombinant soluble LOX-1, FEBS J. 276 (2009) 4909–4920. doi:10.1111/j.1742-4658.2009.07190.x.

[60] S. Chakraborty, Y. Cai, M.A. Tarr, Mapping oxidations of apolipoprotein B-100 in human low-density lipoprotein by liquid chromatography-tandem mass spectrometry, Anal. Biochem. 404 (2010) 109–117. doi:10.1016/j.ab.2010.05.005.

[61] L. Reynolds, R.S. Mulik, X. Wen, A. Dilip, I.R. Corbin, Low-density lipoprotein-mediated delivery of docosahexaenoic acid selectively kills murine liver cancer cells, Nanomedicine. 9 (2014) 2123–2141. doi:10.2217/NNM.13.187.

[62] T. Tagami, T. Ozeki, DDS technology of nano/micro particles and clinical application, Organ Biol. 24 (2017) 54–60.

[63] L.M. Russell, C.M. Dawidczyk, C. Kim, P.C. Searson, J.H. Park, K.H. Lee, M.G. Pomper, State-of-the-art in design rules for drug delivery platforms: Lessons learned from FDA-approved nanomedicines, J. Control. Release. 187 (2014) 133–144. doi:10.1016/j.jconrel.2014.05.036.

[64] C.R. Safinya, K.K. Ewert, Liposomes derived from molecular vases, Nature. 489 (2012) 372–374. doi:10.1038/489372b.

[65] D.A. Chappell, G.L. Fry, M.A. Waknitz, J.J. Berns, Ligand size as a determinant for catabolism by the low density lipoprotein (LDL) receptor pathway. A lattice model for LDL binding., J. Biol. Chem. 266 (1991) 19296–19302.

[66] C. Gan, K. Wang, Q. Tang, Y. Chen, Comparative investigation on the sizes and scavenger receptor binding of human native and modified lipoprotein particles with atomic force microscopy, J. Nanobiotechnology. 16 (2018) 1–11. doi:10.1186/s12951-018-0352-3.

[67] C. Huang, J.T. Mason, Geometric packing constraints in egg phosphatidylcholine vesicles., Proc. Natl. Acad. Sci. 75 (1978) 308–310. doi:10.1073/pnas.75.1.308.

[68] D.Y. Li, Y.C. Zhang, M.I. Philips, T. Sawamura, J.L. Mehta, Upregulation of endothelial receptor for oxidized low-density lipoprotein (LOX-1) in cultured human coronary artery endothelial cells by angiotensin II type 1 receptor activation., Circ. Res. 84 (1999) 1043–1049. http://www.ncbi.nlm.nih.gov/pubmed/10325241.

[69] C. Yuan, J. Furlong, P. Burgos, L.J. Johnston, The Size of Lipid Rafts: An Atomic Force Microscopy Study of Ganglioside GM1 Domains in Sphingomyelin/DOPC/Cholesterol Membranes, Biophys. J. 82 (2002) 2526–2535. doi:10.1016/S0006-3495(02)75596-3.

[70] Y. Obata, Y. Onuki, H. Sano, P. Opanasopit, K. Takayama, T. Ngawhirunpat, S. Kato, S. Duangjit, T. Miyoshi, Comparative Study of Novel Ultradeformable Liposomes: Menthosomes, Transfersomes and Liposomes for Enhancing Skin Permeation of Meloxicam, Biol. Pharm. Bull. 37 (2013) 239–247. doi:10.1248/bpb.b13-00576.

[71] K. Sakai-Kato, Y. Takechi-Haraya, Analytical Methods for Physicochemical Properties of Lipid Membrane Nanovesicles, Bunseki Kagaku. 67 (2018) 1–9.

[72] R.A. Mukhamadiyarov, E.A. Senokosova, S.S. Krutitsky, D. V. Voevoda, I.A. Pyshnaya, V. V. Ivanov, M.J. Lewis, I. Khaliulin, Size-Dependent Ability of Liposomes to Accumulate in the Ischemic Myocardium and Protect the Heart, J. Cardiovasc. Pharmacol. 72 (2018) 143–152. doi:10.1097/FJC.0000000000000606.

[73] T.L. Nguyen, T.H. Nguyen, D.H. Nguyen, Development and In Vitro Evaluation of Liposomes Using Soy Lecithin to Encapsulate Paclitaxel, Int. J. Biomater. 2017 (2017) 1–7. doi:10.1155/2017/8234712.

[74] R.A. Petros, J.M. DeSimone, Strategies in the design of nanoparticles for therapeutic applications, Nat. Rev. Drug Discov. 9 (2010) 615–627. doi:10.1038/nrd2591.

[75] B. Yameen, W. Il Choi, C. Vilos, A. Swami, J. Shi, O.C. Farokhzad, Insight into nanoparticle cellular uptake and intracellular targeting, J. Control. Release. 190 (2014) 485–499. doi:10.1016/j.jconrel.2014.06.038.

[76] C. He, Y. Hu, L. Yin, C. Tang, C. Yin, Effects of particle size and surface charge on cellular uptake and biodistribution

of polymeric nanoparticles, Biomaterials. 31 (2010) 3657–3666. doi:10.1016/j.biomaterials.2010.01.065.

[77] J. Zhao, M.H. Stenzel, Entry of nanoparticles into cells: the importance of nanoparticle properties, Polym. Chem. 9 (2018) 259–272. doi:10.1039/C7PY01603D.

[78] J.K. Vasir, V. Labhasetwar, Quantification of the force of nanoparticle-cell membrane interactions and its influence on intracellular trafficking of nanoparticles, Biomaterials. 29 (2008) 4244–4252. doi:10.1016/j.biomaterials.2008.07.020.

[79] J.L. Mehta, D. Li, Identification, regulation and function of a novel lectin-like oxidized low-density lipoprotein receptor, J. Am. Coll. Cardiol. 39 (2002) 1429–1435. doi:10.1016/S0735-1097(02)01803-X.

[80] M. Chen, T. Masaki, T. Sawamura, LOX-1, the receptor for oxidized low-density lipoprotein identified from endothelial cells: implications in endothelial dysfunction and atherosclerosis, Pharmacol. Ther. 95 (2002) 89–100. doi:10.1016/S0163-7258(02)00236-X.

[81] M. Kapoor, D.J. Burgess, Efficient and safe delivery of siRNA using anionic lipids: Formulation optimization studies, Int. J. Pharm. 432 (2012) 80–90. doi:10.1016/j.ijpharm.2012.04.058.

[82] B. Hu, D. Li, T. Sawamura, J.L. Mehta, Oxidized LDL through LOX-1 modulates LDL-receptor expression in human coronary artery endothelial cells., Biochem. Biophys. Res. Commun. 307 (2003) 1008–12.

[83] M. Akagi, S. Kanata, S. Mori, H. Itabe, T. Sawamura, C. Hamanishi, Possible involvement of the oxidized low-density lipoprotein/lectin-like oxidized low-density lipoprotein receptor-1 system in pathogenesis and progression of human osteoarthritis, Osteoarthr. Cartil. 15 (2007) 281–290. doi:10.1016/j.joca.2006.07.010.

[84] D. Li, L. Liu, H. Chen, T. Sawamura, S. Ranganathan, J.L. Mehta, LOX-1 mediates oxidized low-density lipoprotein-induced expression of matrix metalloproteinases in human coronary artery endothelial cells, Circulation. 107 (2003) 612–617. doi:10.1161/01.CIR.0000047276.52039.FB.

[85] J. Hinagata, M. Kakutani, T. Fujii, T. Naruko, N. Inoue, Y. Fujita, J.L. Mehta, M. Ueda, T. Sawamura, Oxidized LDL receptor LOX-1 is involved in neointimal hyperplasia after balloon arterial injury in a rat model, Cardiovasc. Res. 69 (2006) 263–271. doi:10.1016/j.cardiores.2005.08.013.

[86] K. Sugimoto, T. Ishibashi, T. Sawamura, N. Inoue, M. Kamioka, H. Uekita, H. Ohkawara, T. Sakamoto, N. Sakamoto, Y. Okamoto, Y. Takuwa, A. Kakino, Y. Fujita, T. Tanaka, T. Teramoto, Y. Maruyama, Y. Takeishi, LOX-1-MT1-MMP axis is crucial for RhoA and Rac1 activation induced by oxidized low-density lipoprotein in endothelial cells, Cardiovasc. Res. 84 (2009) 127–136. doi:10.1093/cvr/cvp177.

[87] Y. Delneste, G. Magistrelli, J.F. Gauchat, J.F. Haeuw, J.P. Aubry, K. Nakamura, N. Kawakami-Honda, L. Goetsch, T. Sawamura, J.Y. Bonnefoy, P. Jeannin, Involvement of LOX-1 in dendritic cell-mediated antigen cross-presentation, Immunity. 17 (2002) 353–362. doi:10.1016/S1074-7613(02)00388-6.

[88] D. Li, V. Williams, L. Liu, H. Chen, T. Sawamura, F. Romeo, J.L. Mehta, Expression of lectin-like oxidized low-density lipoprotein receptors during ischemia-reperfusion and its role in determination of apoptosis and left ventricular dysfunction, J. Am. Coll. Cardiol. 41 (2003) 1048–1055. doi:10.1016/S0735-1097(02)02966-2.

[89] N. Nakamura, A. Shuyama, S. Hojyo, M. Shimokawa, K. Miyamoto, T. Kawashima, M. Aosasa, H. Horiuchi, S.

Furusawa, H. Matsuda, Establishment of a chicken monoclonal antibody panel against mammalian prion protein., J. Vet. Med. Sci. 66 (2004) 807–814. doi:10.1292/jvms.66.807.

[90] H. Matsuda, T. Sawamura, Chicken-derived Anti-lox-1 Antibody, WO/2010/147171 A1, 2010. https://patents.google.com/patent/WO2010147171A1/ja?oq=WO%2F2010%2F147171.

[91] H. Shirai, A. Kidera, H. Nakamura, Structural classification of CDR-H3 in antibodies., FEBS Lett. 399 (1996) 1–8.

[92] L. Wu, K. Oficjalska, M. Lambert, B.J. Fennell, A. Darmanin-Sheehan, D. Ni Shuilleabhain, B. Autin, E. Cummins, L. Tchistiakova, L. Bloom, J. Paulsen, D. Gill, O. Cunningham, W.J.J. Finlay, Fundamental Characteristics of the Immunoglobulin VH Repertoire of Chickens in Comparison with Those of Humans, Mice, and Camelids, J. Immunol. 188 (2012) 322–333. doi:10.4049/jimmunol.1102466.

[93] H.H. Shih, C. Tu, W. Cao, A. Klein, R. Ramsey, B.J. Fennell, M. Lambert, D. Ní Shúilleabháin, B. Autin, E. Kouranova, S. Laxmanan, S. Braithwaite, L. Wu, M. Ait-Zahra, A.J. Milici, J.A. Dumin, E.R. LaVallie, M. Arai, C. Corcoran, J.E. Paulsen, D. Gill, O. Cunningham, J. Bard, L. Mosyak, W.J.J. Finlay, An ultra-specific avian antibody to phosphorylated tau protein reveals a unique mechanism for phosphoepitope recognition, J. Biol. Chem. 287 (2012) 44425–44434. doi:10.1074/jbc.M112.415935.

[94] J.C. Almagro, G. Raghunathan, E. Beil, D.J. Janecki, Q. Chen, T. Dinh, A. Lacombe, J. Connor, M. Ware, P.H. Kim, R. V. Swanson, J. Fransson, Characterization of a high-affinity human antibody with a disulfide bridge in the third complementarity-determining region of the heavy chain, J. Mol. Recognit. 25 (2012) 125–135. doi:10.1002/jmr.1168.

[95] L.A. Kelly, S. Mezulis, C. Yates, M. Wass, M. Sternberg, The Phyre2 web portal for protein modelling, prediction, and analysis, Nat. Protoc. 10 (2015) 845–858. doi:10.1038/nprot.2015-053.

[96] D. Xu, Y. Zhang, Improving the physical realism and structural accuracy of protein models by a two-step atomic-level energy minimization, Biophys. J. 101 (2011) 2525–2534. doi:10.1016/j.bpj.2011.10.024.

[97] B. Webb, A. Sali, Comparative Protein Structure Modeling Using MODELLER., Curr. Protoc. Protein Sci. 86 (2016) 2.9.1-2.9.37. doi:10.1002/cpps.20.

[98] M. Shen, A. Sali, Statistical potential for assessment and prediction of protein structures, Protein Sci. 15 (2006) 2507–2524. doi:10.1110/ps.062416606.

[99] B.G. Pierce, Y. Hourai, Z. Weng, Accelerating protein docking in ZDOCK using an advanced 3D convolution library, PLoS One. 6 (2011). doi:10.1371/journal.pone.0024657.

[100] B.G. Pierce, K. Wiehe, H. Hwang, B.H. Kim, T. Vreven, Z. Weng, ZDOCK server: Interactive docking prediction of protein-protein complexes and symmetric multimers, Bioinformatics. 30 (2014) 1771–1773. doi:10.1093/bioinformatics/btu097.

[101] G. Vriend, C. Sander, Quality control of protein models: directional atomic contact analysis, J.Appl.Cryst. 26 (1993) 47–60.

[102] G. Vriend, WHAT IF: a molecular modeling and drug design program., J. Mol. Graph. 8 (1990) 52–56, 29.

[103] J. Mintseris, B. Pierce, K. Wiehe, R. Anderson, R. Chen, Z. Weng, Integrating statistical pair potentials into protein

complex prediction, Proteins Struct. Funct. Bioinforma. 69 (2007) 511–520. doi:10.1002/prot.21502.

[104] O.L. Francone, M. Tu, L.J. Royer, J. Zhu, K. Stevens, J.J. Oleynek, Z. Lin, L. Shelley, T. Sand, Y. Luo, C.D. Kane, The hydrophobic tunnel present in LOX-1 is essential for oxidized LDL recognition and binding, J. Lipid Res. 50 (2008) 546–555. doi:10.1194/jlr.m800474-jlr200.

[105] S. Biocca, F. Iacovelli, S. Matarazzo, G. Vindigni, F. Oteri, A. Desideri, M. Falconi, Molecular mechanism of statin-mediated LOX-1 inhibition, Cell Cycle. 14 (2015) 1583–1595. doi:10.1080/15384101.2015.1026486.

[106] M.A. Larkin, G. Blackshields, N.P. Brown, R. Chenna, P.A. Mcgettigan, H. McWilliam, F. Valentin, I.M. Wallace, A. Wilm, R. Lopez, J.D. Thompson, T.J. Gibson, D.G. Higgins, Clustal W and Clustal X version 2.0, Bioinformatics. 23 (2007) 2947–2948. doi:10.1093/bioinformatics/btm404.

公表論文

(1) DOPG small unilamellar vesicles function as nano-carriers targeting the clustered lectin-like oxidized LDL receptor (LOX-1) on the cell surface.

Ohta T, Yamada R, Fujita S, Takahata T, Shiba K, Machida S, Tate S

J Drug Deliv Sci Technol 51 (2019) 327-336.

参考論文

(1) Study on an inactivation evaluation method of cleaning processes for biopharmaceuticals.
Kaminagayoshi T, Takenaka K, Ohta T, Doi T, Sadamitsu M, Omori S, Tsuji S, Miko Y, Shirokizawa O, and Walsh A
BioPharm International 31 (9) (2018) 22-28.